Buckling and post-buckling of variable stiffness plates with cutouts by a single-domain Ritz method

A. Milazzo[1], G. Guarino[1], and V. Gulizzi[1]

[1]Department of Engineering, University of Palermo, Viale delle Scienze, Bldg 8, 90128 Palermo - Italy

Abstract

Structural components with variable stiffness can provide better performances with respect to classical ones and offer an enlarged design space for their optimization. They are attractive candidates for advanced lightweight structural applications whose functionalities often impose the presence of cutouts that requires accurate and effective analysis for their design. In the present work, a single-domain Ritz formulation is proposed, implemented and validated for the analysis of buckling and post-buckling behaviour of variable stiffness plates with cutouts. The plate model is based on the first-order shear deformation theory with nonlinear von Karman strain-displacement relationships. The plate generalized displacements are approximated with trial functions built as products of one-dimensional Legendre orthogonal polynomials. The non linear governing equations system is then deduced from the stationarity of the energy functional; the involved matrices are numerically computed by a special integration algorithm based on the implicit description of the cutout via suitable level-set functions. The formulation has been implemented in a computer code which has been used to validate the method through comparison with literature solutions for variable angle tow laminates with circular cutouts. Several investigations on buckling and post-buckling behaviour of variable angle tow composite plates with cutouts having different shapes and dimensions are then presented to illustrate the approach capabilities, provide benchmark results and point out features and design opportunities of the variable stiffness concept for the buckling and post-buckling design of advanced lightweight structures.

1 Introduction

The availability of advanced manufacturing technologies [1], such as Automated Fiber Placement, Continuous Tow Sharing, Automated Tape Layup, 3D Printing, enables the efficient construction of variable stiffness composite structures [2]. In aerospace, automotive and naval fields this open towards new optimized design of lightweight components with high structural performances especially with regard to their dynamic, buckling and post-buckling behaviour that can be meaningfully enhanced [3, 4]. Often, these structural components have complex geometries and can present cut-out openings (e.g. windows, holes, access cut-outs, etc) due to functional and weight requirements. Thus, to fully exploit the advantages and opportunities of the variable stiffness concept, it is crucial to develop accurate and efficient tools for the structural modeling, analysis and optimization of components designed under this paradigm. Starting from the pioneering works of Hyer and coworkers [5, 6], many studies have been performed in the literature by using the finite element method (FEM), see e.g. [7, 8, 9, 10, 11, 12, 13], only to cite some recent works, that largely contributed to the understanding of variable stiffness composites behaviour as regard stress distributions, buckling, vibrations and failure.~~Starting from the pioneering works of Hyer and coworkers [5, 6], many studies have been performed in the literature by using the finite element method (FEM), see e.g. [7, 8, 9], only to cite some recent works, that largely contributed to the understanding of variable stiffness composites behaviour.~~ However, in standard finite element formulations, the orientation of the fibers is typically assumed constant inside each element. This inherently leads to a non-smooth fiber path and may produce loss in accuracy, unless extremely refined mesh size is employed with the consequent rapid growth of the required computational resources. This deficiency can be overcome by advanced FEM formulation such as those based on isogeometric analysis, see e.g. [14], that generally are not available in industrial commercial software. Numerical approaches alternative to finite elements for variable stiffness composite analyses have been proposed in the context of meshless methods [15, 16, 17] and generalized differential quadrature method [18, 19, 20, 21, 22]. On the other hand, semi-analytical methods can be recognized as computationally efficient to model variable stiffness composite structures especially in view of optimization procedure application. In particular, the Rayleigh-Ritz method has been extensively employed to investigate the buckling and post-buckling behaviour of intact variable stiffness plate by Weaver and co-workers [23, 24, 25, 26, 27], by Guimares et al. [28], by Vescovini and Dozio [29] and by Milazzo and co-workers [30, 31, 32, 33]. Also cracked variable stiffness plates have been investigated for buckling and free vibrations by the eXtended Ritz method [34, 35].

Focusing on the structural analysis of composite components with cut-outs, the literature survey

reveals that FEM is the widely employed approach [6, 36, 37, 38, 39, 40]; problem solutions have been also proposed using the isogeometric analysis formulation [41], the moving least square meshless method [17], the Ritz method coupled with the energy effect removal technique [42], the multiregion plate assembly Ritz method [43] and the Discontinuous Galerkin method [44, 45, 46, 47].

The remarks reported above shows that buckling and post-buckling analysis of variable stiffness plate with cut-outs is a primary concern in the design of future lightweight structures. In this framework semi-analytical approaches can significantly contribute as they can provide benchmark solutions and efficient alternatives to finite elements especially in the preliminary design phase and in optimization procedures.

In view of this, in the present work a novel single-domain Ritz approach is proposed for the buckling and post-buckling analysis of quadrilateral variable stiffness composite plates with cut-outs and elastically restrained edges. The cut-out is geometrically described in implicit form by suitable level set function. The plate structural model is based on the first order shear deformation theory accounting for geometrical nonlinearity under the von Karman nonlinear plate assumptions. To apply the Ritz method, the problem primary variable, namely the plate midplane translation and the plate section rotations, are approximated by a set of trial functions built as products of one-dimensional orthogonal Legendre polynomials. The plate governing equations in terms of the primary variables unknown Ritz coefficients are then determined by the stationarity condition of the total energy potential, which provides the nonlinear resolving system. The characteristic matrices of the resolving system are computed using a special integration technique that, based on the implicit description of the cut-out via a suitably-defined level set function, allows for an accurate evaluation of domain integrals over the plate domain. This is the principal novelty and the core of the proposed novel Ritz approach. Validation results and studies to show the potential of the method are finally presented.

2 Formulation

Consider a quadrilateral layered composite plate containing a cut-out. Let the plate have variable stiffness arising from material and lay-up characteristics (e.g. variable angle tow laminates) and thickness distribution The plate behaviour is described in the framework of the first order shear deformation theory (FSDT), considering nonlinear geometrical description based on the von Karman assumptions holding for moderately large deflections and rotations [48].

2.1 Geometry definition and reference systems

Let the plate be referred to a Cartesian coordinate system with the x_1 and x_2 coordinates spanning its mid-plane and the x_3-axis directed along its thickness. Let Ω denotes the quadrilateral domain occupied by the plate in the x_1x_2 plane and let $\partial\Omega$ be its boundary. A natural coordinate system $\xi\eta$ is also introduced that maps the square domain $[-1,1]\times[-1,1]$ onto the domain Ω via standard bilinear shape functions [49]. A geometrical sketch of the plate and the introduced reference systems is presented in Fig. 1.

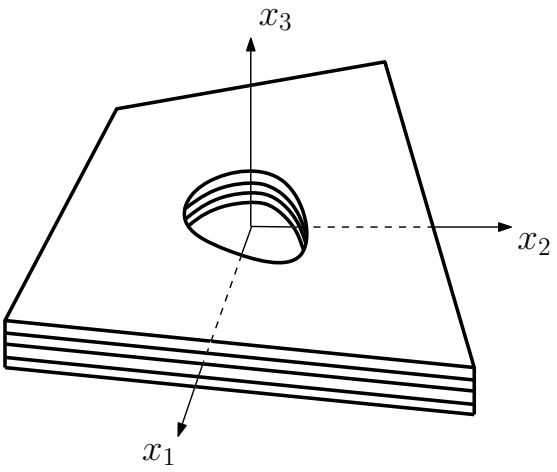

(a) Plate 3D geometry

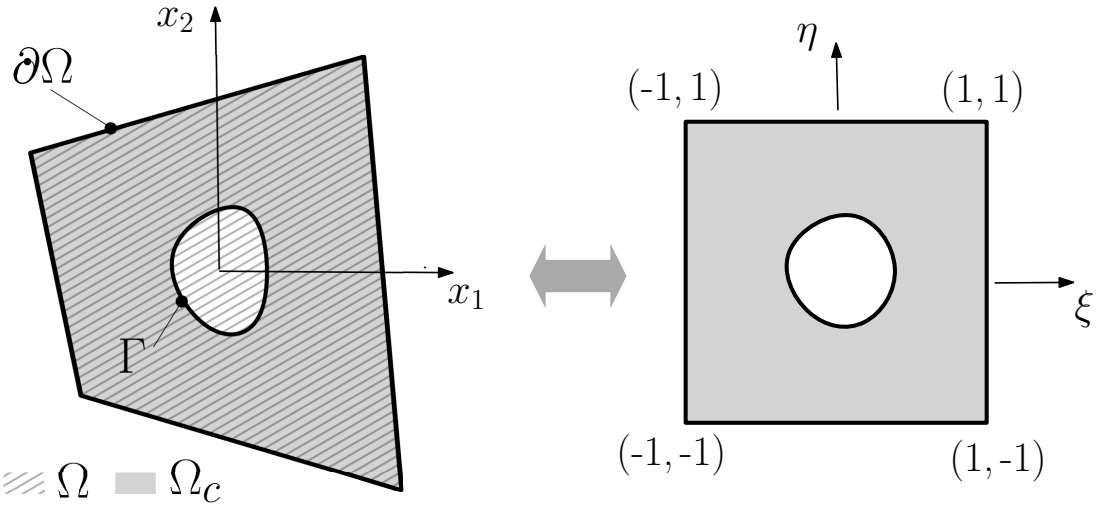

(b) Plate domains, boundaries and reference systems.

Figure 1: Plate geometry and reference systems.

The plate cut-out is implicitly-defined via a level set function ϕ of the x_1 and x_2 coordinates [45]

and then the reference domain Ω_c of the plate with cut-out is given by

$$\Omega_c \equiv \{(x_1, x_2) \in \Omega \mid \phi(x_1, x_2) < 0\} \tag{1}$$

while its boundary $\partial\Omega_c$ is defined as

$$\partial\Omega_c \equiv \{(x_1, x_2) \in \partial\Omega \mid \phi(x_1, x_2) < 0\} \cup \Gamma_c \tag{2}$$

where $\Gamma_c \equiv \{(x_1, x_2) \in \Omega \mid \phi(x_1, x_2) = 0\}$ denotes the boundary of the cut-out. It is observed that for a plate without cut-out, Ω_c and $\partial\Omega_c$ coincide with Ω and $\partial\Omega$, respectively.

The plate is subjected to external loads consisting of: *(i)* forces per unit area applied to the plate domain Ω_c with components directed along the cartesian reference axes and described by the vector $\boldsymbol{q} = \left\{ q_1 \quad q_2 \quad q_3 \right\}^T$; *(i)* moments per unit area applied to the plate domain Ω_c which are collected in the vector $\boldsymbol{m} = \left\{ m_1 \quad m_2 \right\}^T$ whose components are the moments around the in-plane cartesian reference axes; *(iii)* forces per unit length applied along the boundary $\partial\Omega_c$ whose components along the cartesian reference axes are collected in the vector $\overline{\boldsymbol{N}} = \left\{ \overline{N}_{n1} \quad \overline{N}_{n2} \quad \overline{N}_{n3} \right\}^T$; *(iv)* moments per unit length around the in-plane cartesian reference axes, which are applied along the boundary $\partial\Omega_c$ and whose components are collected in the vector $\overline{\boldsymbol{M}} = \left\{ \overline{M}_{n1} \quad \overline{M}_{n2} \right\}^T$.

The plate boundary $\partial\Omega_c$ is elastically restrained by translational springs with stiffness k_1^u, k_2^u and k_3^u along the cartesian reference axes and by rotational springs with stiffness k_1^ψ and k_2^ψ around the x_2 and x_1 axis. It is remarked that a zero spring stiffness value corresponds to free variable boundary conditions whereas an infinite spring stiffness value fully constrains the corresponding degree of freedom; basing on this observation the plate kinematical boundary conditions can be numerically enforced via the penalty concept [50].

Eventually, the plate can exhibit an initial imperfection described by a given transverse deflection $\overline{w}$ of its mid-plane with respect to the flat configuration.

2.2 Kinematical model

The plate displacement field $\boldsymbol{d}^T = \left\{ d_1(x_1, x_2, x_3) \quad d_2(x_1, x_2, x_3) \quad d_3(x_1, x_2, x_3) \right\}^T$ is written as

$$\boldsymbol{d} = \boldsymbol{u} + x_3 \boldsymbol{L}\boldsymbol{\psi} + \overline{\boldsymbol{u}} \tag{3}$$

where $\boldsymbol{u}^T = \begin{Bmatrix} u_1(x_1,x_2) & u_2(x_1,x_2) & u_3(x_1,x_2) \end{Bmatrix}$ is the mid-plane translations vector, $\boldsymbol{\psi}^T = \begin{Bmatrix} \psi_1(x_1,x_2) & \psi_2(x_1,x_2) \end{Bmatrix}$ is the plate rotations vector and the vector $\overline{\boldsymbol{u}}^T = \begin{Bmatrix} 0 & 0 & \overline{w}(x_1,x_2) \end{Bmatrix}^T$ accounts for the initial imperfection. In Eq. (3) the matrix operator $\boldsymbol{L}$ is defined as

$$\boldsymbol{L}^T = \begin{bmatrix} 1 & 0 & 0 \\ 0 & 1 & 0 \end{bmatrix} \tag{4}$$

Collecting the Green's strains into the in-plane and out-of-plane components vectors $\boldsymbol{e}_p = \begin{Bmatrix} e_{11} & e_{22} & e_{12} \end{Bmatrix}^T$ and $\boldsymbol{e}_n = \begin{Bmatrix} e_{13} & e_{23} \end{Bmatrix}^T$, respectively, the nonlinear strain-displacements relations under the von Karman assumptions are given by

$$\boldsymbol{e}_p = \boldsymbol{\mathscr{D}}_p \boldsymbol{u} + \frac{1}{2} \left(\boldsymbol{\mathscr{D}}_p \otimes u_3 \right) \boldsymbol{\mathscr{D}}_n \boldsymbol{u} + \left(\boldsymbol{\mathscr{D}}_p \otimes \overline{w} \right) \boldsymbol{\mathscr{D}}_n \boldsymbol{u} + x_3 \boldsymbol{\mathscr{D}}_p \boldsymbol{L} \boldsymbol{\psi} = \boldsymbol{\varepsilon}_0 + x_3 \boldsymbol{\kappa} \tag{5a}$$

$$\boldsymbol{e}_n = \boldsymbol{L}^T \boldsymbol{\mathscr{D}}_n \boldsymbol{u} + \boldsymbol{\psi} = \boldsymbol{\gamma} \tag{5b}$$

where the symbol $\otimes$ denotes the Kronecker's product and the following differential operators are introduced

$$\boldsymbol{\mathscr{D}}_p = \begin{bmatrix} \dfrac{\partial}{\partial x} & 0 & 0 \\ 0 & \dfrac{\partial}{\partial y} & 0 \\ \dfrac{\partial}{\partial y} & \dfrac{\partial}{\partial x} & 0 \end{bmatrix} \qquad \boldsymbol{\mathscr{D}}_n = \begin{bmatrix} 0 & 0 & \dfrac{\partial}{\partial x} \\ 0 & 0 & \dfrac{\partial}{\partial y} \\ 0 & 0 & 0 \end{bmatrix} \tag{6}$$

It is worth noting that in Eqs. (5) $\boldsymbol{\varepsilon}_0$ is the generalized in-plane strains vector, $\boldsymbol{\kappa}$ is the curvatures vector and $\boldsymbol{\gamma}$ is the shear strains vector.

2.3 Plate constitutive law

According to the kinematical model introduced in the preceding subsection, the mechanical state is described by the 2nd Piola-Kirchoff stress vector whose components obey the material constitutive law for generalized elastic orthotopic materials. Assuming a plane-stress state, namely $\sigma_{33} = 0$, at the plate point

of coordinates (x_1, x_2, x_3), the constitutive law reads as

$$\boldsymbol{\sigma} = \left\{ \begin{array}{c} \boldsymbol{\sigma}_p \\ \hline \boldsymbol{\sigma}_n \end{array} \right\} = \left\{ \begin{array}{c} \sigma_{11} \\ \sigma_{22} \\ \sigma_{12} \\ \hline \sigma_{31} \\ \sigma_{32} \end{array} \right\} = \left[\begin{array}{ccc|cc} Q_{11} & Q_{12} & Q_{13} & 0 & 0 \\ Q_{12} & Q_{22} & Q_{23} & 0 & 0 \\ Q_{13} & Q_{23} & Q_{33} & 0 & 0 \\ \hline 0 & 0 & 0 & Q_{44} & Q_{45} \\ 0 & 0 & 0 & Q_{45} & Q_{55} \end{array} \right] \left\{ \begin{array}{c} \varepsilon_{11} \\ \varepsilon_{22} \\ \varepsilon_{12} \\ \hline \varepsilon_{31} \\ \varepsilon_{32} \end{array} \right\} = \left[\begin{array}{c|c} \boldsymbol{Q}_p & \mathbf{0} \\ \hline \mathbf{0} & \boldsymbol{Q}_n \end{array} \right] \left\{ \begin{array}{c} \boldsymbol{\varepsilon}_p \\ \hline \boldsymbol{\varepsilon}_n \end{array} \right\} = \boldsymbol{Q}\boldsymbol{\varepsilon} \tag{7}$$

where the Q_{ij} are the material stiffness coefficients [48].

The plate internal actions corresponding to this stress state are the membrane stress resultants per unit length $\boldsymbol{N} = \int_h \boldsymbol{\sigma}_p dx_3$, the transverse stress resultants per unit length $\boldsymbol{T} = \int_h \boldsymbol{\sigma}_n dx_3$ and the moments per unit length $\boldsymbol{M} = \int_h x_3 \boldsymbol{\sigma}_p dx_3$. They are linked to the generalized strains defined in Eqs. (5) by the following constitutive equations

$$\left\{ \begin{array}{c} \boldsymbol{N} \\ \boldsymbol{M} \\ \boldsymbol{T} \end{array} \right\} = \left[\begin{array}{ccc} \boldsymbol{A} & \boldsymbol{B} & \mathbf{0} \\ \boldsymbol{B} & \boldsymbol{D} & \mathbf{0} \\ \mathbf{0} & \mathbf{0} & \boldsymbol{G} \end{array} \right] \left\{ \begin{array}{c} \boldsymbol{\varepsilon}_0 \\ \boldsymbol{\kappa} \\ \boldsymbol{\gamma} \end{array} \right\} \tag{8}$$

In the Eq. (8), $\boldsymbol{A}$, $\boldsymbol{B}$, $\boldsymbol{D}$ and $\boldsymbol{G}$ are the extensional, bending–extension coupling, bending and shear stiffness matrices, respectively, which are defined as [48]

$$\langle \boldsymbol{A}(x_1, x_2),\, \boldsymbol{B}(x_1, x_2),\, \boldsymbol{D}(x_1, x_2) \rangle = \int_{h(x_1, x_2)} \langle 1,\, x_3,\, x_3^2 \rangle\; \boldsymbol{Q}_p(x_1, x_2, x_3)\; dx_3 \tag{9}$$

$$\boldsymbol{G}(x_1, x_2) = \boldsymbol{F}(x_1, x_2) \int_{h(x_1, x_2)} \boldsymbol{Q}_n(x_1, x_2, x_3)\; dx_3 \tag{10}$$

where $\boldsymbol{F}$ is a 2×2 matrix containing the shear correction factors [51]. It is remarked that the stiffness matrices are generally function of the in-plane coordinates x_1 and x_2 depending on material and thickness distributions. In the framework of stiffness variations related to material distributions, let us focus on variable angle tow (VAT) laminates. They are obtained by stacking fiber-reinforced composite plies whose fibres are laid at a variable angle in the lamina plane; thus, the fibre orientation angle ϑ depends on the in-plane coordinates, namely $\vartheta = \vartheta(x_1,\, x_2)$, and consequently at a ply level it results $Q_{ij} = Q_{ij}(x_1, x_2)$. In the present work, the case of ϑ linearly varying along a baseline $\mathbf{r}$ lying in the $x_1 x_2$ plane and inclined

by the angle ϑ_0 with respect to the x_1 axis is considered, namely

$$\vartheta(r) = \vartheta_0 + \frac{1}{L_r}\left(\vartheta_B - \vartheta_A\right)|r| + \vartheta_A \tag{11}$$

where ϑ_A and ϑ_B are the fibre orientation angles with respect to the baseline at the point A and B, respectively, whose distance along the baseline is L_r (see Fig. 2). If the point A corresponds to the

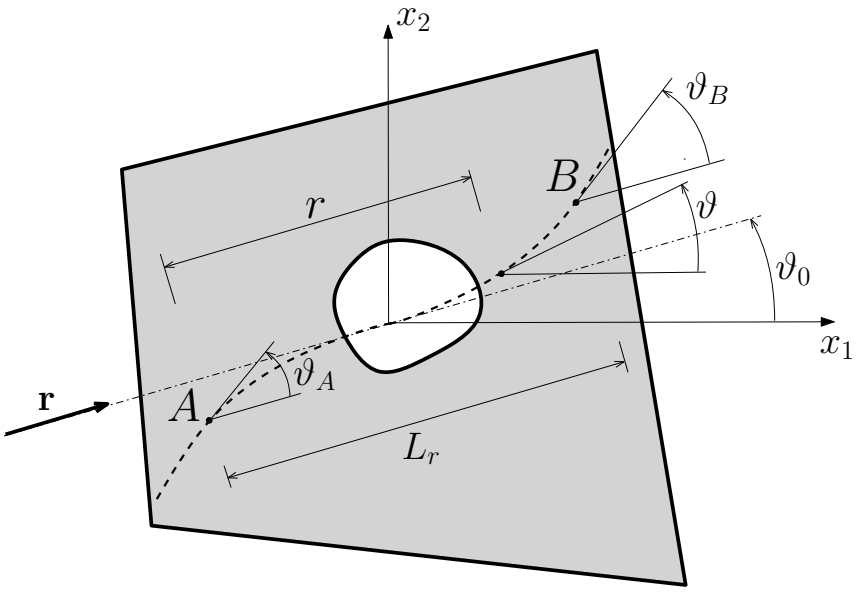

Figure 2: Definition of fibre path for a variable angle tow lamina.

projection of the plate center and the point B belong to a plate edge, fibre paths described by Eq. (11) correspond to those originally proposed by Gürdal and Olmedo [52] and they are briefly denoted as $\vartheta_0\langle\vartheta_A|\vartheta_B\rangle$. It is clear that straight fibers laminates can be analyzed as a subcase of VAT layups when $\theta_A = \theta_B$.

2.4 Variational statement and governing equations

Assuming that the strain–displacement relationships, namely Eqs. (5), and the plate constitutive relationships, namely Eqs (8), are fulfilled, the plate governing equations are obtained by the stationarity conditions of the following functional Π with respect to the problem primary variable that are the mid-

plane translations $\boldsymbol{u}$ and the transverse section rotations $\boldsymbol{\psi}$ [53]

$$\begin{aligned}\Pi = \int_{\Omega_c} \frac{1}{2}\Big[\boldsymbol{\varepsilon}_0^T \boldsymbol{A}\boldsymbol{\varepsilon}_0 + \boldsymbol{\varepsilon}_0^T \boldsymbol{B}\boldsymbol{\kappa} + \boldsymbol{\kappa}^T \boldsymbol{B}\boldsymbol{\varepsilon}_0 + \boldsymbol{\kappa}^T \boldsymbol{D}\boldsymbol{\kappa} + \boldsymbol{\gamma}^T \boldsymbol{G}\boldsymbol{\gamma}\Big] d\Omega - \\ \int_{\Omega_c} \Big[\boldsymbol{u}^T \boldsymbol{q} + \boldsymbol{\psi}^T \boldsymbol{m}\Big]\, d\Omega - \int_{\partial\Omega_c} \Big[\boldsymbol{u}^T \overline{\boldsymbol{N}} + \boldsymbol{\psi}^T \overline{\boldsymbol{M}}\Big]\, d\partial\Omega + \\ \int_{\partial\Omega_c} \frac{1}{2}\Big[\boldsymbol{u}^T \boldsymbol{k}_u \boldsymbol{u} + \boldsymbol{\psi}^T \boldsymbol{k}_\psi \boldsymbol{\psi}\Big]\, d\partial\Omega\end{aligned} \tag{12}$$

In the Eq. (12) $\boldsymbol{k}_u$ and $\boldsymbol{k}_\psi$ are 3×3 and 2×2 diagonal matrices collecting the translational and rotational boundary springs stiffnesses, respectively.

2.5 Ritz solution

The solution of the plate problem outlined in the previous section is obtained through the Ritz method, which is implemented as described in the following.

2.5.1 Primary variables approximation

The unknown generalized displacement χ, with $\chi \in \{u_1,\, u_2,\, u_3,\, \psi_1,\, \psi_2\}$, is approximated as

$$\chi = \sum_{m=0}^{M_\chi} \sum_{n=0}^{N_\chi} p^\chi_{nN_\chi+m} c^\chi_{nN_\chi+m} = \boldsymbol{p}_\chi \boldsymbol{c}_\chi \tag{13}$$

where $\boldsymbol{p}_\chi$ is the row vector collecting the trial functions $p^\chi_{nN_\chi+m}$ and $\boldsymbol{c}_\chi$ is the column vector collecting the corresponding Ritz unknown coefficients $c^\chi_{nN_\chi+m}$. In the present work, the trial functions are chosen as

$$p^\chi_{nN_\chi+m} = \mathscr{P}_m(\xi)\, \mathscr{P}_n(\eta) \tag{14}$$

where $\mathscr{P}_k(\zeta)$ is the Legendre polynomial of k-th order. Accordingly to Eq. (13), the plate generalized displacements, which are the problem primary variables, are written in compact matrix form as

$$\boldsymbol{u} = \begin{bmatrix} \boldsymbol{p}_{u_1} & \boldsymbol{0} & \boldsymbol{0} \\ \boldsymbol{0} & \boldsymbol{p}_{u_2} & \boldsymbol{0} \\ \boldsymbol{0} & \boldsymbol{0} & \boldsymbol{p}_{u_3} \end{bmatrix} \begin{Bmatrix} \boldsymbol{c}_{u_1} \\ \boldsymbol{c}_{u_2} \\ \boldsymbol{c}_{u_3} \end{Bmatrix} = \begin{bmatrix} \boldsymbol{P}_{u_1} \\ \boldsymbol{P}_{u_2} \\ \boldsymbol{P}_{u_3} \end{bmatrix} \boldsymbol{U} = \boldsymbol{P}_U\, \boldsymbol{U} \tag{15a}$$

$$\boldsymbol{\psi} = \begin{bmatrix} \boldsymbol{p}_{\psi_1} & \boldsymbol{0} \\ \boldsymbol{0} & \boldsymbol{p}_{\psi_2} \end{bmatrix} \begin{Bmatrix} \boldsymbol{c}_{\psi_1} \\ \boldsymbol{c}_{\psi_2} \end{Bmatrix} = \boldsymbol{P}_\Psi\, \boldsymbol{\Psi} \tag{15b}$$

2.5.2 Strain-displacement relationships

The plate generalized strain are then expressed as

$$\boldsymbol{\varepsilon}_0 = \boldsymbol{\mathcal{B}}_U^p\, \boldsymbol{U} + \frac{1}{2}\, \boldsymbol{\mathcal{B}}_U^{nl}\, \boldsymbol{U} + \overline{\boldsymbol{\mathcal{B}}}_U^{nl}\, \boldsymbol{U} \tag{16a}$$

$$\boldsymbol{\kappa} = \boldsymbol{\mathcal{B}}_\Psi^p\, \boldsymbol{\Psi} \tag{16b}$$

$$\boldsymbol{\gamma} = \boldsymbol{\mathcal{B}}_U^n\, \boldsymbol{U} + \boldsymbol{\mathcal{B}}_\Psi^i\, \boldsymbol{\Psi} \tag{16c}$$

where

$$\boldsymbol{\mathcal{B}}_U^p = \boldsymbol{\mathscr{D}}_p \boldsymbol{P}_U \tag{17a}$$

$$\boldsymbol{\mathcal{B}}_\Psi^p = \boldsymbol{\mathscr{D}}_p \boldsymbol{L} \boldsymbol{P}_\Psi \tag{17b}$$

$$\boldsymbol{\mathcal{B}}_U^{nl} = \left[\boldsymbol{\mathscr{D}}_p \otimes (\boldsymbol{P}_{u_3} \boldsymbol{U})\right] \boldsymbol{\mathscr{D}}_n \boldsymbol{P}_U \tag{17c}$$

$$\overline{\boldsymbol{\mathcal{B}}}_U^{nl} = \left(\boldsymbol{\mathscr{D}}_p \otimes \overline{w}\right) \boldsymbol{\mathscr{D}}_n \boldsymbol{P}_U \tag{17d}$$

$$\boldsymbol{\mathcal{B}}_U^n = \boldsymbol{L}^T \boldsymbol{\mathscr{D}}_n \boldsymbol{P}_U \tag{17e}$$

$$\boldsymbol{\mathcal{B}}_\Psi^i = \boldsymbol{P}_\Psi \tag{17f}$$

2.5.3 Nonlinear governing equations

Substituting Eqs. (16) into Eq. (12) provides the Ritz-discretized form of the functional Π whose stationarity conditions with respect to $\boldsymbol{U}$ and $\boldsymbol{\Psi}$ return the plate governing equations in the form of the following nonlinear system [53]

$$\left(\boldsymbol{K}_0 + \boldsymbol{K}_1 + \boldsymbol{K}_2 + \overline{\boldsymbol{K}}_0 + \overline{\boldsymbol{K}}_1 + \boldsymbol{R}\right) \boldsymbol{X} = \boldsymbol{F} \tag{18}$$

where the Ritz unknown coefficients vector $\boldsymbol{X}^T = \left\{ \boldsymbol{U}^T \quad \boldsymbol{\Psi}^T \right\}$ has been introduced. The matrices and vectors appearing in Eq. (18) are defined as

$$\boldsymbol{K}_0 = \int_{\Omega_e} \left[\begin{array}{c|c} {\boldsymbol{\mathcal{B}}_U^p}^T \boldsymbol{A}\, \boldsymbol{\mathcal{B}}_U^p + {\boldsymbol{\mathcal{B}}_U^n}^T \boldsymbol{G}\, \boldsymbol{\mathcal{B}}_U^n & {\boldsymbol{\mathcal{B}}_U^p}^T \boldsymbol{B}\, \boldsymbol{\mathcal{B}}^p \Psi + {\boldsymbol{\mathcal{B}}_U^n}^T \boldsymbol{G}\, \boldsymbol{\mathcal{B}}_\Psi^i \\ \hline {\boldsymbol{\mathcal{B}}_\Psi^p}^T \boldsymbol{B}\, \boldsymbol{\mathcal{B}}_U^p + {\boldsymbol{\mathcal{B}}_\Psi^i}^T \boldsymbol{G}\, \boldsymbol{\mathcal{B}}_U^n & {\boldsymbol{\mathcal{B}}_\Psi^p}^T \boldsymbol{D}\, \boldsymbol{\mathcal{B}}_\Psi^p + {\boldsymbol{\mathcal{B}}_\Psi^i}^T \boldsymbol{G}\, \boldsymbol{\mathcal{B}}_\Psi^i \end{array}\right] d\Omega \tag{19a}$$

$$\boldsymbol{K}_1 = \int_{\Omega_c} \left[\begin{array}{c|c} \frac{1}{2}{\mathcal{B}_U^p}^T \boldsymbol{A}\, \mathcal{B}_U^{nl} + {\mathcal{B}_U^{nl}}^T \boldsymbol{A}\, \mathcal{B}_U^p & {\mathcal{B}_U^{nl}}^T \boldsymbol{B}\, \mathcal{B}_\Psi^p \\ \hline \frac{1}{2}{\mathcal{B}_\Psi^p}^T \boldsymbol{B}\, \mathcal{B}_U^{nl} & \boldsymbol{0} \end{array}\right] d\Omega \tag{19b}$$

$$\boldsymbol{K}_2 = \int_{\Omega_c} \left[\begin{array}{c|c} \frac{1}{2}{\mathcal{B}_U^{nl}}^T \boldsymbol{A}\, \mathcal{B}_U^{nl} & \boldsymbol{0} \\ \hline \boldsymbol{0} & \boldsymbol{0} \end{array}\right] d\Omega \tag{19c}$$

$$\overline{\boldsymbol{K}}_0 = \int_{\Omega_c} \left[\begin{array}{c|c} {\mathcal{B}_U^p}^T \boldsymbol{A}\, \overline{\mathcal{B}}_U^{nl} + {\overline{\mathcal{B}}_U^{nl}}^T \boldsymbol{A}\, \mathcal{B}_U^p + {\overline{\mathcal{B}}_U^{nl}}^T \boldsymbol{A}\, \overline{\mathcal{B}}_U^{nl} & {\overline{\mathcal{B}}_U^{nl}}^T \boldsymbol{B}\, \mathcal{B}_\Psi^p \\ \hline {\mathcal{B}_\Psi^p}^T \boldsymbol{B}\, \overline{\mathcal{B}}_U^{nl} & \boldsymbol{0} \end{array}\right] d\Omega \tag{19d}$$

$$\overline{\boldsymbol{K}}_1 = \int_{\Omega_c} \left[\begin{array}{c|c} {\mathcal{B}_U^{nl}}^T \boldsymbol{A}\, \overline{\mathcal{B}}_U^{nl} + \frac{1}{2}{\overline{\mathcal{B}}_U^{nl}}^T \boldsymbol{A}\, \mathcal{B}_U^{nl} & \boldsymbol{0} \\ \hline \boldsymbol{0} & \boldsymbol{0} \end{array}\right] d\Omega \tag{19e}$$

$$\boldsymbol{R} = \int_{\partial\Omega_c} \left[\begin{array}{c|c} \boldsymbol{P}_u^T \boldsymbol{k}_u \boldsymbol{P}_u & \boldsymbol{0} \\ \hline \boldsymbol{0} & \boldsymbol{P}_\Psi^T \boldsymbol{k}_\psi \boldsymbol{P}_\Psi \end{array}\right] d\partial\Omega \tag{19f}$$

$$\boldsymbol{F} = \int_{\Omega_c} \left\{\begin{array}{c} \boldsymbol{P}_u^T \boldsymbol{q} \\ \hline \boldsymbol{P}_\Psi^T \boldsymbol{m} \end{array}\right\} d\Omega + \int_{\partial\Omega_c} \left\{\begin{array}{c} \boldsymbol{P}_u^T \overline{\boldsymbol{N}} \\ \hline \boldsymbol{P}_\Psi^T \overline{\boldsymbol{M}} \end{array}\right\} d\partial\Omega \tag{19g}$$

It is worth noting that overlined matrices refer to the contributions associated with the plate initial imperfection and that the matrices $\boldsymbol{K}_2$, $\boldsymbol{K}_1$ and $\overline{\boldsymbol{K}}_1$ depend on the unknown vector $\boldsymbol{X}$. Solution of Eq. (18) is achieved by incremental-iterative procedures, which need the computation of the associated Jacobian matrix defined as

$$\boldsymbol{J} = \boldsymbol{K}_0 + \boldsymbol{K}_1^t + \boldsymbol{K}_2^t + \boldsymbol{K}_G + \overline{\boldsymbol{K}}_0 + \overline{\boldsymbol{K}}_1^t + \boldsymbol{R} \tag{20}$$

where

$$\boldsymbol{K}_1^t = \int_{\Omega_c} \left[\begin{array}{c|c} {\mathcal{B}_U^p}^T \boldsymbol{A}\, \mathcal{B}_U^{nl} + {\mathcal{B}_U^{nl}}^T \boldsymbol{A}\, \mathcal{B}_U^p & {\mathcal{B}_U^{nl}}^T \boldsymbol{B}\, \mathcal{B}_\Psi^p \\ \hline {\mathcal{B}_\Psi^p}^T \boldsymbol{B}\, \mathcal{B}_U^{nl} & \boldsymbol{0} \end{array}\right] d\Omega \tag{21a}$$

$$\boldsymbol{K}_2^t = \int_{\Omega_c} \left[\begin{array}{c|c} \boldsymbol{\mathcal{B}}_U^{nl\,T}\,\boldsymbol{A}\,\boldsymbol{\mathcal{B}}_U^{nl} & \boldsymbol{0} \\ \hline \boldsymbol{0} & \boldsymbol{0} \end{array}\right] d\Omega \tag{21b}$$

$$\boldsymbol{K}_G = \int_{\Omega_c} \left[\begin{array}{c|c} \boldsymbol{\mathcal{B}}_U^{n\,T}\,\widehat{\boldsymbol{N}}\,\boldsymbol{\mathcal{B}}_U^{n} & \boldsymbol{0} \\ \hline \boldsymbol{0} & \boldsymbol{0} \end{array}\right] d\Omega \tag{21c}$$

$$\overline{\boldsymbol{K}}_1^t = \int_{\Omega_c} \left[\begin{array}{c|c} \boldsymbol{\mathcal{B}}_U^{nl\,T}\,\boldsymbol{A}\,\overline{\boldsymbol{\mathcal{B}}}_U^{nl} + \overline{\boldsymbol{\mathcal{B}}}_U^{nl\,T}\,\boldsymbol{A}\,\boldsymbol{\mathcal{B}}_U^{nl} & \boldsymbol{0} \\ \hline \boldsymbol{0} & \boldsymbol{0} \end{array}\right] d\Omega \tag{21d}$$

(21e)

being

$$\widehat{\boldsymbol{N}} = \begin{bmatrix} N_{11} & N_{12} & 0 \\ N_{12} & N_{22} & 0 \\ 0 & 0 & 0 \end{bmatrix} \tag{22}$$

For more details on the derivation of Eqs. (18) and (20) the reader is referred to Refs [49, 50].

2.5.4 Linear buckling equations

The linear buckling eigenvalue problem associated with Eq. (18) is written as [54]

$$\left(\boldsymbol{K}_0 + \boldsymbol{R} + \lambda \boldsymbol{K}_G\right) \boldsymbol{X} = \boldsymbol{0} \tag{23}$$

where the eigenvalue λ is the load multiplier and the eigenvectors $\boldsymbol{X}$ contain the Ritz coefficients of the buckling mode. Note that in Eq. (23), the matrix $\boldsymbol{K}_G$ is computed with the membrane stress distribution of the pre-buckled state, which is determined by linear analysis assuming that it varies in a self-similar manner as the load grows.

3 Integration

The terms introduced in Eqs.(19) and (21) are defined as the integrals of the trial functions and the stiffness coefficient matrices over the domain and the boundaries of the plate. When a simple quadrilateral plate is considered, these integrals are computed by using standard tensor-product Gaussian quadrature rules defined in the $[-1,1] \times [-1,1]$ domain spanned by the natural coordinates ξ and η. However, a different strategy is needed when the plate contains a cut-out. Several approaches may be employed in this case:

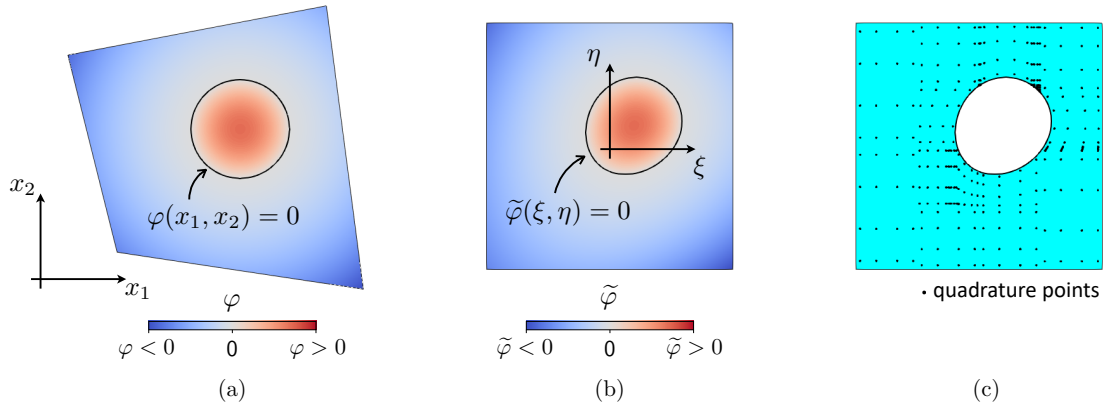

Figure 3: (a) Level set function defined in the Cartesian reference system. (b) Level set function defined in the natural reference system. (c) Location of the quadrature points.

examples proposed in the literature include partitioning the domain using a hierarchical quad-tree data structure, see e.g. [55], or using the quadrature rules associated with an explicit parametrization of the cut-out [42]. Here, the integration algorithm proposed in Ref. [56] is used as it allows evaluating high-order accurate quadrature rules for implicitly-defined domains and boundaries and has been successfully employed in 2D and 3D numerical applications involving both fluid [57, 58, 59, 60] and solid/structural mechanics [45, 46, 61]. In particular, the considered cut-outs are implicitly defined via a level set function of the Cartesian coordinates x_1 and x_2, i.e. $\varphi = \varphi(x_1, x_2)$. By using the bilinear shape functions, the level set function φ is expressed in terms of the natural coordinates ξ and η to obtain $\widetilde{\varphi}(\xi, \eta) \equiv \varphi(x_1(\xi, \eta), x_2(\xi, \eta))$, which is then used to provide the quadrature rules. An example of the domain quadrature rule for a quadrilateral plate with a circular cut-out is reported in Fig.(3), which shows the plots of the level set functions φ and $\widetilde{\varphi}$ in figures (a) and (b), respectively, and the location of the quadrature points in figure (c).

4 Numerical Results

A computer code based on the formulation outlined in Sec. 2 and the integration scheme described in Sec.3 has been implemented and employed to carry out the numerical results presented in this section. These results refer to square VAT composite plates with cut-outs. The plates have edge length $L = 0.254\,\mathrm{m}$ and 16–layer layup. The plies elastic properties in the orthotropic material reference system are given as $E_1 = 181.0\,\mathrm{GPa}$, $E_2 = 10.273\,\mathrm{GPa}$, $G_{13} = G_{12} = G_{23} = 7.1705\,\mathrm{GPa}$, $\nu_{12} = 0.28$, being E_i the Young's moduli, G_{ij} the shear moduli and ν_{ij} the Poisson's coefficients. The plies thickness is assumed

constant and equal to 0.1272 mm with a corresponding whole laminate thickness $h = 2.0352$ mm. Different variable stiffness laminates are considered built with VAT plies having linearly varying fibre orientation angle, see Eq. (11), and $[\pm(\theta_0\langle\theta_A/\theta_B\rangle)]_{4S}$ layup. The plates are simply-supported along all the edges with free bending and torsional rotations. In the model, these boundary conditions are simulated by a penalty technique implemented with suitable values of the boundary spring stiffness corresponding to the constrained degrees of freedom. In particular, the boundary spring stiffness values are set proportional to 10^s times the material maximum Young modulus, with $4 \leq s \leq 7$ as suggested in Ref. [50]. The plates undergo uniform compression displacements $u_1 = \Delta$ applied along the edges $x_1 = \pm L/2$; this loading condition corresponds to an average edge force resultant per unit length $\bar{N}_{11}$ that is defined as

$$\bar{N}_{11} = \frac{1}{L}\int_{-L/2}^{L/2} N_{11}(\pm L/2, x_2)dx_2 \tag{24}$$

Additionally, a reference value for the buckling load is also introduced as the buckling load $\bar{N}^{cr}_{11_{iso}}$ corresponding to an homogeneous quasi isotropic plate without cut-out having the same dimension and boundary conditions of the analyzed plates and whose Poisson's coefficient and Young modulus are evaluated as $\nu_{iso} = 0.296$ and $E_{iso} = 69.668$ GPa [25]. An explanatory sketch of the plate geometry with a central circular cut-out and of the loading conditions is given in Fig. 4.

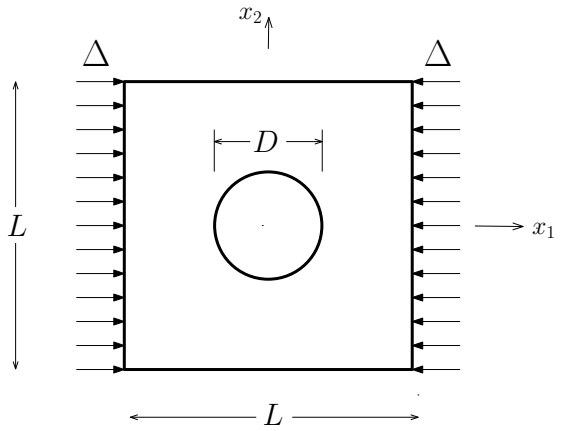

Figure 4: Plate geometry and loading condition.

4.1 Convergence analysis and validation

Preliminarily, convergence studies are performed for both plate buckling and post-buckling referring to a Ritz approximation scheme corresponding to Eq. (15) where $M_\chi = N_\chi = N$ and $\chi \in \{u_1, u_2, u_3, \psi_1, \psi_2\}$. After the convergence analyses, the approach has been validated by assessing its accuracy against available

literature results. It is pointed out that due to the huge number of possible VAT plate configurations, for the sake of brevity and without affecting the drawn considerations, the presented results are limited to some cases which are deemed representative of the method behaviour.

4.1.1 Buckling

The results of Fig. 5 refer to the convergence of the first four buckling modes with respect to the number of employed trial functions for the plates with $[\pm(90\langle 0/75\rangle)]_{4S}$ layup and a central circular cut-out of diameter $D/L = 0.2$ and $D/L = 0.6$.

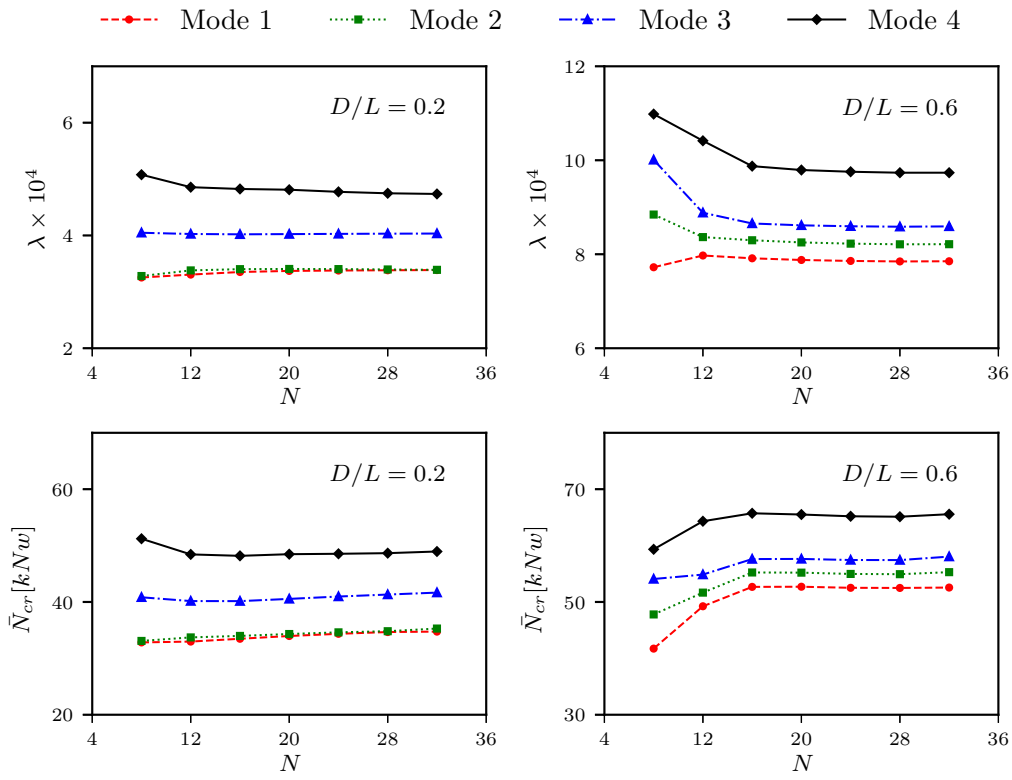

Figure 5: Convergence studies for the $[\pm(90\langle 0/45\rangle)]_{4S}$ square plate exhibiting a central circular cut of diameter $D/L = 0.2$ and $D/L = 0.6$.

The analysis of the data shows a good convergence behaviour for both the buckling eigenvalue and the corresponding buckling average edge force resultant $\bar{N}_{11}^{cr}$; as expected in Ritz approaches convergence of the buckling force is slightly slower than that of displacements. Similar results have been also obtained for different cut-out geometries (elliptical, square) and plate layups. All of the convergence analyses suggest that choosing $N = 24$ provides converged results and then this approximation scheme will be

retained in the following buckling analyses focusing, as usual, on the first buckling mode.

Validation of the present method has been carried out by comparing the present results with solutions available in the literature, which also allows for an assessment of the solution accuracy. Table 1 lists the normalized buckling load for plates with different VAT layups and centered circular cut-outs of different diameter D. Comparison of the present results with those of Ref. [17] and FEM ones by ABAQUS [17] shows good agreement demonstrating the capability of the proposed approach to accurately evaluate buckling loads of variable stiffness plates with cut-outs. Additionally, it is observed that the present results have been obtained with a relatively low number of degrees of freedom, which indicates a good effectiveness of the approach.

Table 1: Buckling loads for compressed square plates with a centered circular cutout.

		$\bar{N}_{11}^{cr}/\bar{N}_{11_{iso}}^{cr}$		
Layup	D/L	Present	Ref. [17]	FEM [17]
$[\pm\langle 90\langle 0/75\rangle\rangle]_{4S}$	0.0	2.19	2.22	2.19
	0.2	2.10	2.13	2.09
	0.4	2.06	2.09	2.01
	0.6	2.16	2.22	2.12
$[\pm\langle 0\langle 60/30\rangle\rangle]_{4S}$	0.0	1.09	1.17	1.17
	0.2	0.93	1.02	0.99
	0.4	1.02	1.08	1.03
	0.6	1.46	1.56	1.43
$[\pm\langle 45\langle 15/0\rangle\rangle]_{4S}$	0.0	1.20	1.17	1.15
	0.2	1.03	1.06	1.04
	0.4	1.05	1.09	1.07
	0.6	1.48	1.54	1.48
$[\pm\langle 90\langle 45/45\rangle\rangle]_{4S}$	0.0	1.21	1.23	1.24
	0.2	1.06	1.12	1.12
	0.4	1.08	1.11	1.11
	0.6	1.45	1.51	1.51

Eventually, to complete the presentation of the approach potential, buckling modes corresponding to the cases analyzed in Table 1 are shown in Fig. 6 observing the ability to capture the modal shape variations with layup and cut-out dimension.

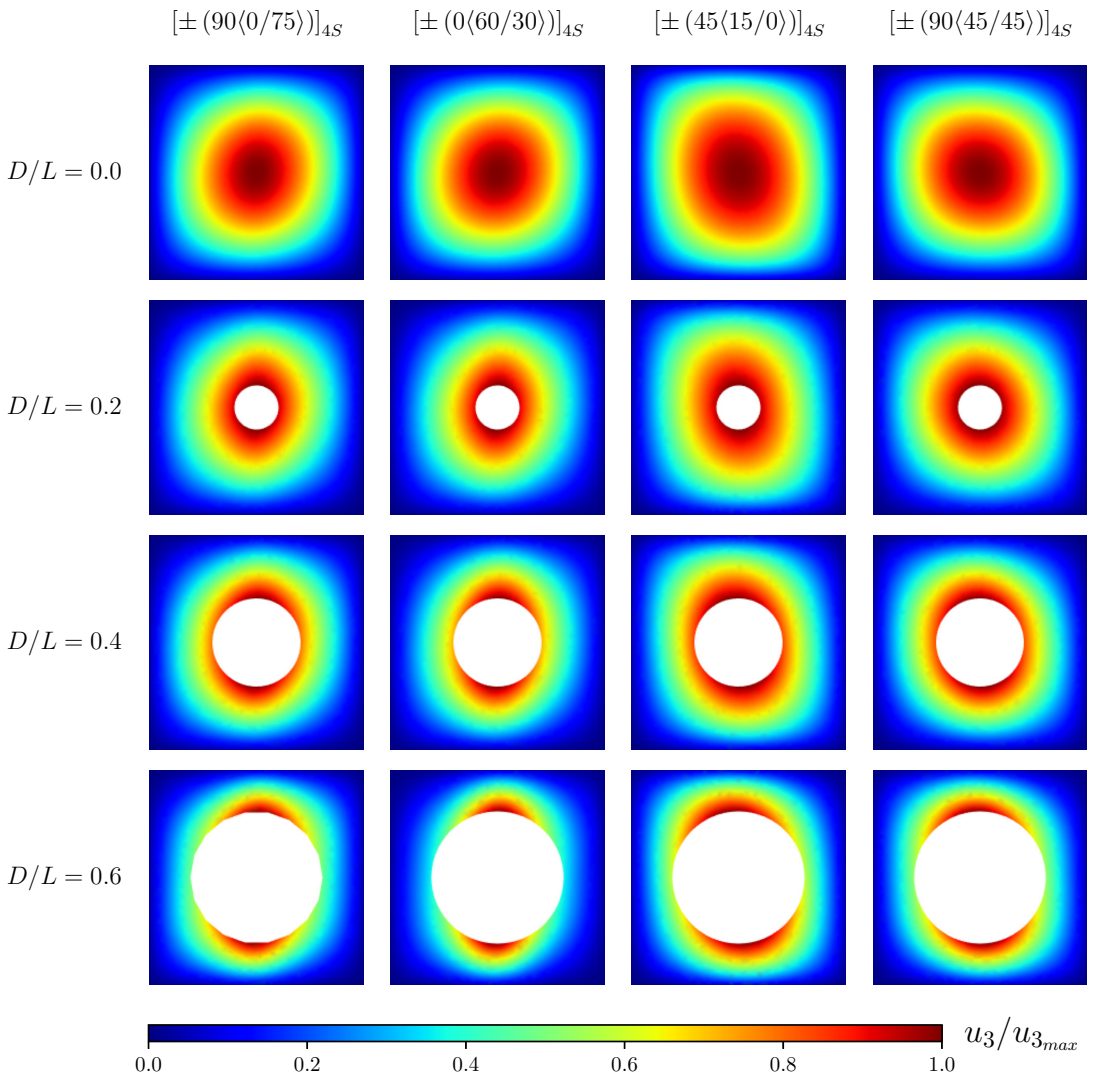

Figure 6: First buckling mode shape for different VAT laminates with a center circular cut-out exhibiting different diameters D.

4.1.2 Post-buckling

The results presented and discussed to illustrate the post-buckling convergence characteristics focus on the $[90 \pm \langle 0|45\rangle]_{4S}$ plate with a $D/L = 0.2$ centered circular cut-out and an initial imperfection corresponding to the first buckling mode shape with amplitude equal to the 0.1 % of the plate thickness. Fig. 7a shows

the equilibrium path for the transverse displacement at cut-out edge, namely at the point of in plane coordinates $(D, 0)$, with respect to the applied normalized compression strain ε_{11} for increasing refined Ritz approximation schemes. On the other hand, Fig. 7b shows the corresponding load-shortening curve in pre- and post-buckling regime. The data suggest effective convergence features of the method for both the primary variables, namely displacements, and stress resultants.

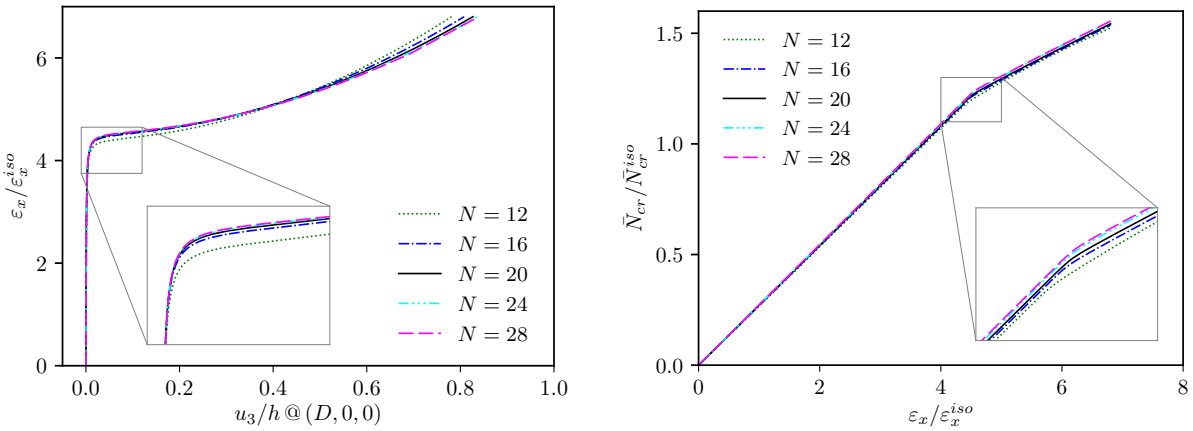

(a) Equilibrium path

(b) Load-end shortening curve

Figure 7: Convergence analysis for the postbukling solution of the $[90 \pm \langle 0|45 \rangle]_{4S}$ plate with a $D/L = 0.2$ centered circular cut-out.

To validate the method for the post-buckling regime, a set of different VAT laminates containing a central circular cut-out with various diameters has been solved assuming an initial imperfection corresponding to the first buckling mode shape with amplitude equal to the 0.1 % of the plate thickness. Fig. 8 shows the comparison of the obtained results with the finite element solutions reported in Ref. [17]. Both equilibrium paths for the maximum transverse displacement and load-shortening curves are reported in Figs. 8a and 8b, respectively.

They show a general good agreement with the finite element data. It is remarked that some results actually refer to straight fibres laminates, straightforwardly solvable by commercial FEM codes; these however have been analyzed employing the numerical procedures developed for the VAT case for code validation purposes.

In conclusion, the performed convergence and accuracy studies, for which representative cases have been illustrated in the preceding paragraphs, enables an appropriate level of confidence in the approach. Thus, it can be employed to ascertain the buckling and post-buckling behaviour of variable stiffness laminates with cut-outs in the context of design and optimization procedures.

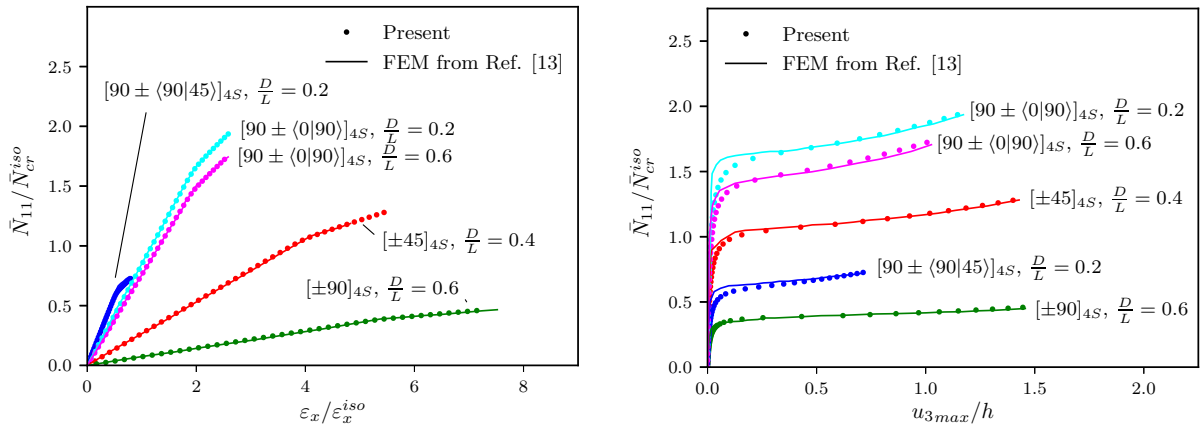

(a) Equilibrium path

(b) Load-end shortening curve

Figure 8: post-buckling solutions for VAT laminates with central circular cut-outs.

4.2 Examples of parametric studies

The proposed method can be used to perform parametric studies [34, 62, 35] to investigate the behaviour of variable stiffness plates with cut-outs and provide data for the selection of effective structural solutions. To show this capability, in the present section some examples are provided considering the variation of the structural performances with respect to different fibre paths used in the laminate layup $[\pm(\theta_0\langle\theta_A/\theta_B\rangle)]_{4S}$; material properties and plate geometry are the same as the analyses presented above.

4.2.1 Buckling

Fig. 9 shows the variation of the buckling load with respect to the plies fibre path for the considered laminates with a central circular cut-out; the reported subplots refer to the plate without cut-out ($D/L = 0.0$) and to the cut-out cases with different diameters ($D/L = 0.2, 0.4, 0.6$). Analogously, Figs. 10 and 11 outline the same kind of results for the case of an elliptical and a square cut-out, respectively, whose geometrical data are sketched in the same figures; once again different dimensions of the cut-out have been considered in the analysis.

The presented results firstly demonstrate the capability of the method to deal with different geometries. Here basic cut-out geometries have been considered, which are described by the level set functions reported in Appendix A; however, also more complex cut-outs can similarly analyzed by suitably defining the corresponding level set functions [56].

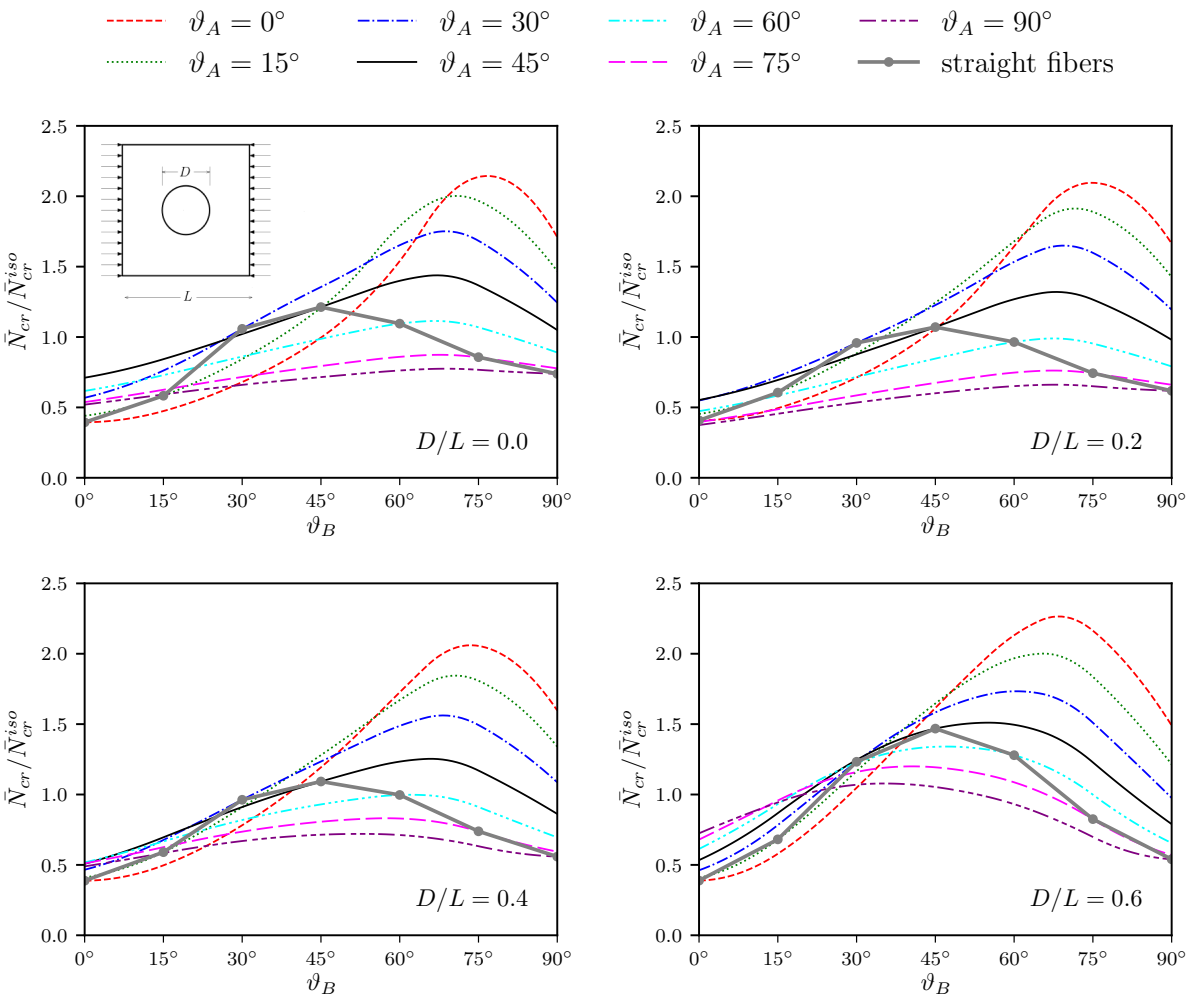

Figure 9: Buckling load for square VAT $[\pm(\theta_0\langle\theta_A|\theta_B\rangle)]_{4S}$ laminates presenting a central circular cut-out.

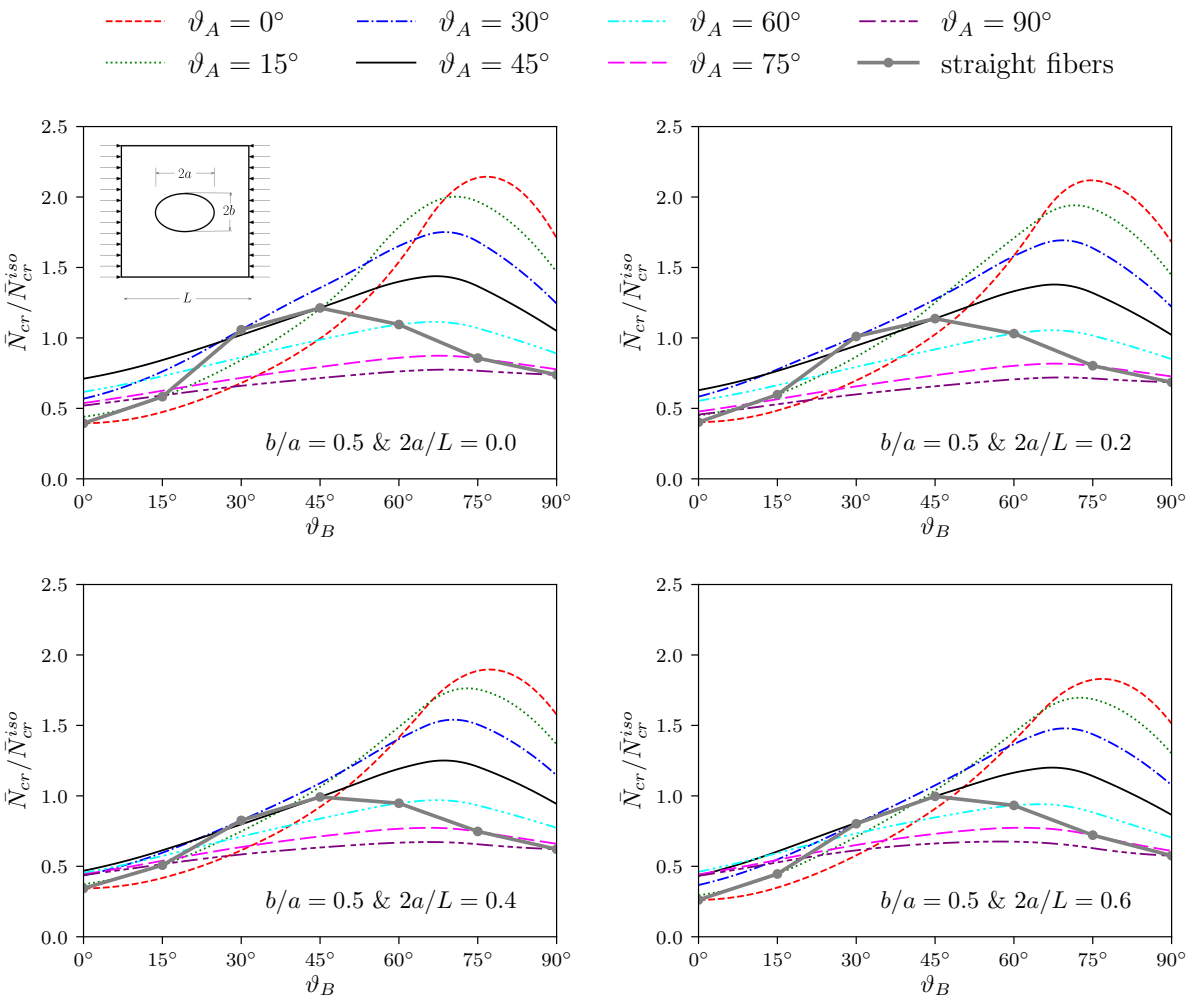

Figure 10: Buckling load for square VAT $[\pm\langle\theta_0\langle\theta_A/|\theta_B\rangle\rangle]_{4S}$ laminates presenting a central elliptical cut-out.

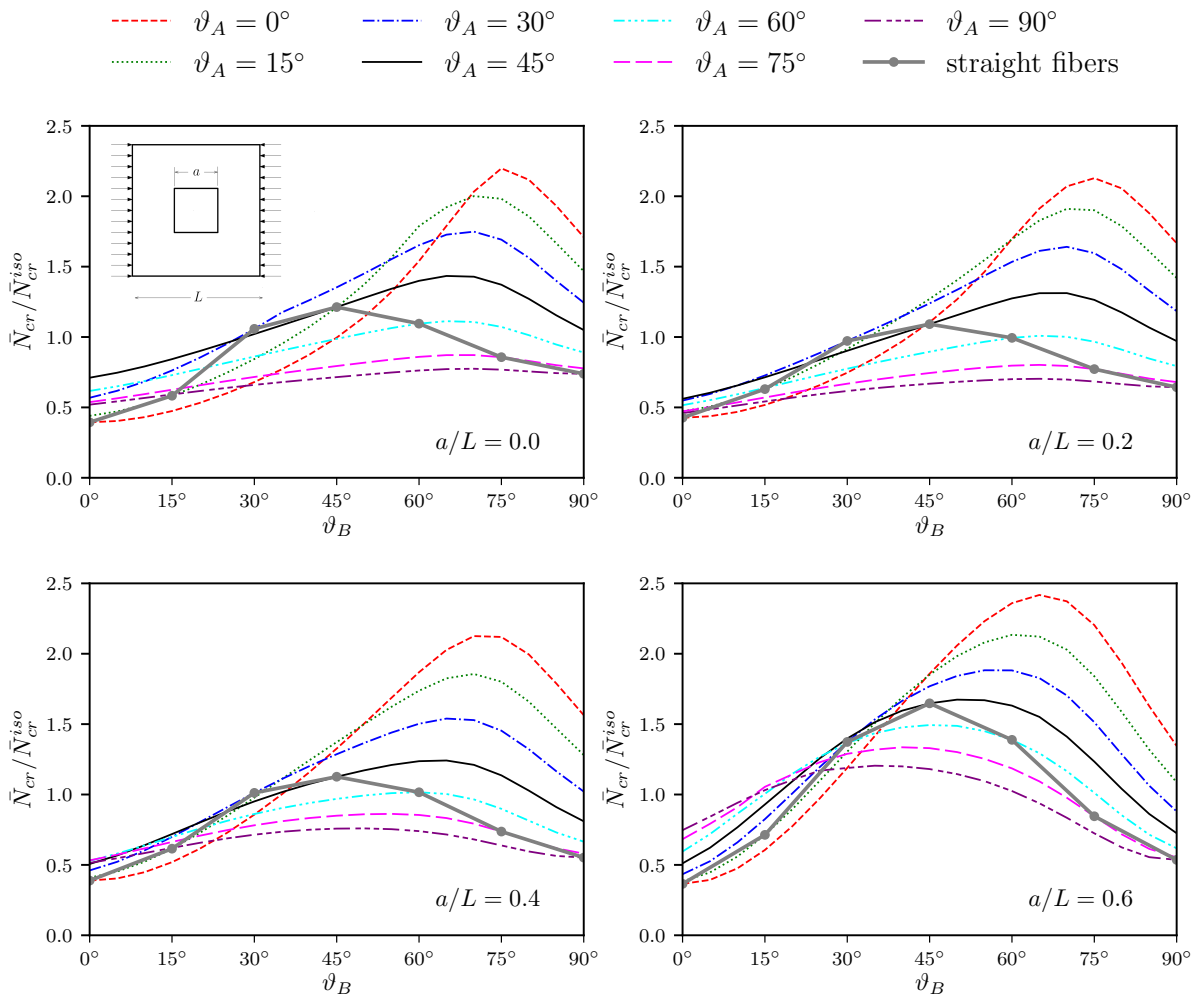

Figure 11: Buckling load for square VAT $[\pm(\theta_0\langle\theta_A|\theta_B\rangle)]_{4S}$ laminates presenting a central square cut-out.

The analysis of these buckling results allows to take some observation on VAT variable stiffness laminates. For all the examined cut-out geometries, the selection of appropriate fibre path generates higher buckling loads with respect to the straight fibre case; in particular higher values of ϑ_B determines a favourable redistribution of the loading stresses with consequent gain in the buckling loads. This behaviour, just evidenced in the literature for plates without cut-outs, is also verified for plates with cut-outs. The dimension of the cut-out affects the buckling load and determines different possible trends relatable to the ply fibre paths. For a given layup configuration, depending on the selected fibre path: *i)* the buckling load initially decreases as the cut-out dimension increases reversing this trend for large dimensions of the cut-out as a result of the stress redistribution and the change of the original plate buckling mode into the buckling of the lateral strips; *ii)* the buckling load monotonically decreases as the cut-out dimension increases. This trends are better illustrated in Fig. 12 for the case of a square cut-out. For example, the cited behaviour trends are verified for the $[90 \pm \langle 30|45\rangle]_{4S}$ and $[90 \pm \langle 30|90\rangle]_{4S}$ laminates whose buckling load for the different cut-out dimensions are marked by circles in the Figure; the corresponding buckling mode shape in terms of transverse displacement fringes are also depicted in the Figure to substantiate the above considerations.

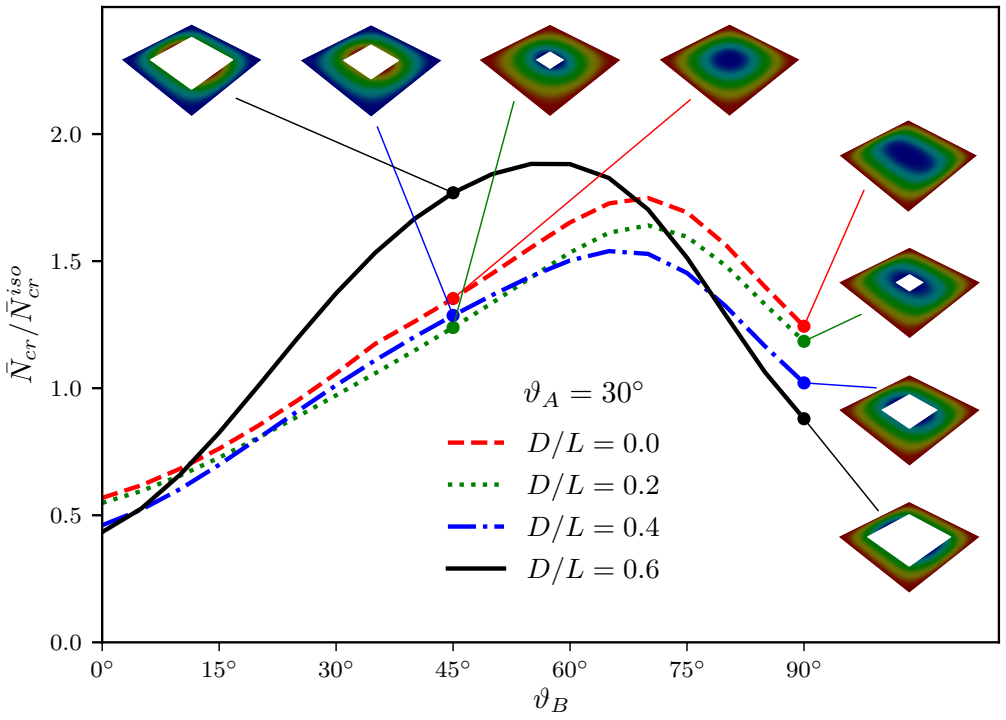

Figure 12: Buckling load for square VAT $[\pm\,(90\langle 30|/\theta_B\rangle)]_{4S}$ laminates presenting a central square cut-out.

4.2.2 Post-buckling

To illustrate the capability of the method, some examples~~An example~~ of post-buckling investigations are ~~is~~ proposed in this section for the VAT laminates with cut-outs of different shape and dimension~~central square cut-out having different edge length a~~. The investigated plate geometry and laminate layups are the same as the previous examples; an initial imperfection corresponding to the first buckling mode shape with amplitude equal to the 0.1 % of the plate thickness has been assumed in the analyses. Fig. 13 shows the load-displacement curves resulting from the analyses for the VAT laminates with a central elliptical cutout having axes ratio $b/a = 0.5$ and different characteristic dimension $2a/L$. Analogously, Fig. 14 shows the load-displacement curves for the case of central square cut-out with different edge length a/L. The results clearly evidence the influence of the fibres pattern on the nonlinear post-buckling response of the plates. Eventually, to exemplify the possible use of the method as a design tool, a ~~The~~ study is performed ~~focusing~~ on the plates stiffness that can be used to connote the performance in post-buckling regime; in particular pre-buckling stiffness K_{pre} and post-buckling stiffness K_{post} are extracted from the computed load versus end-shortening curves [63]. Fig. 15 shows the variation of the K_{pre} and K_{post} with respect to the ply fibre paths for the $[\pm(90\langle\theta_A/\theta_B\rangle)]_{4S}$ laminates; these stiffnesses are normalized by the value of K_{iso} that is the pre-buckling stiffness of the homogeneous quasi isotropic plate without cut-out corresponding to the investigated laminates [25]. Each curve in Fig. 15 describe VAT laminates with fixed value of ϑ_A and varying values of ϑ_B, more in detail ϑ_B varies from 0° at the left end to 90° at the right end. The figure also reports a *baseline* curve relative to classical straight fibres laminates. From the data it is outlined that the variable stiffness concept allows to build laminates that exhibit higher values of the post-buckling stiffness K_{post} with respect to the straight fiber laminate with the same pre-buckling stiffness K_{pre}. This circumstance occurs for plates with and without cut-out and confirms the findings reported in Ref. [25] for intact plates and in Ref. [17] for plates with circular holes. Additionally, as the cut-out dimension grows the pre-buckling stiffness and initial post-buckling stiffness decreases, following trends that are similar to those of plates without cut-outs.

5 Conclusions

A Ritz approach for the buckling and post-buckling analysis of variable stiffness laminated plates with cut-outs has been formulated, implemented and tested. The plate model uses the first order shear deformation

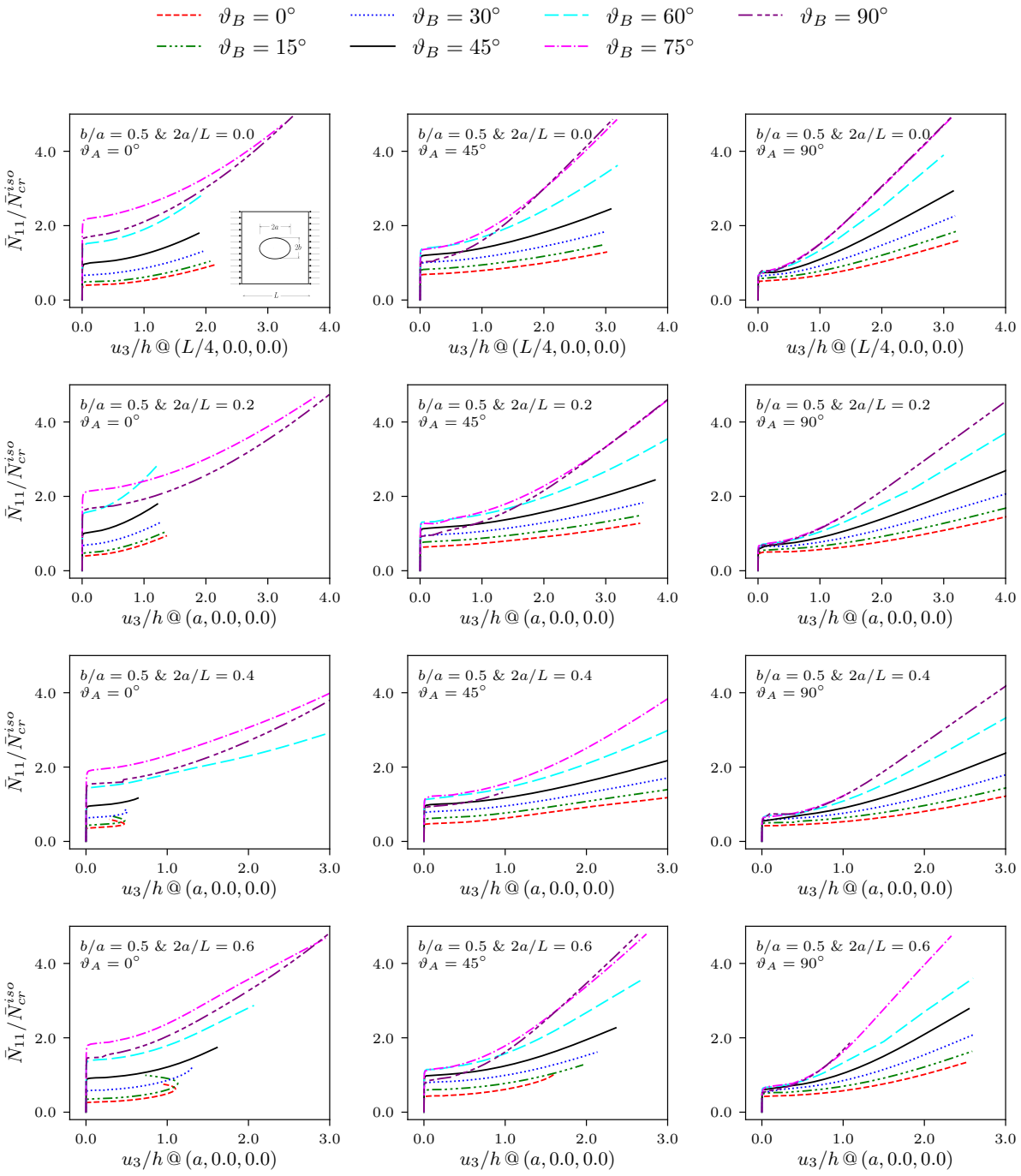

Figure 13: Load-displacement curves for VAT laminates with a central elliptical cut-out having different dimension $2a/L$.

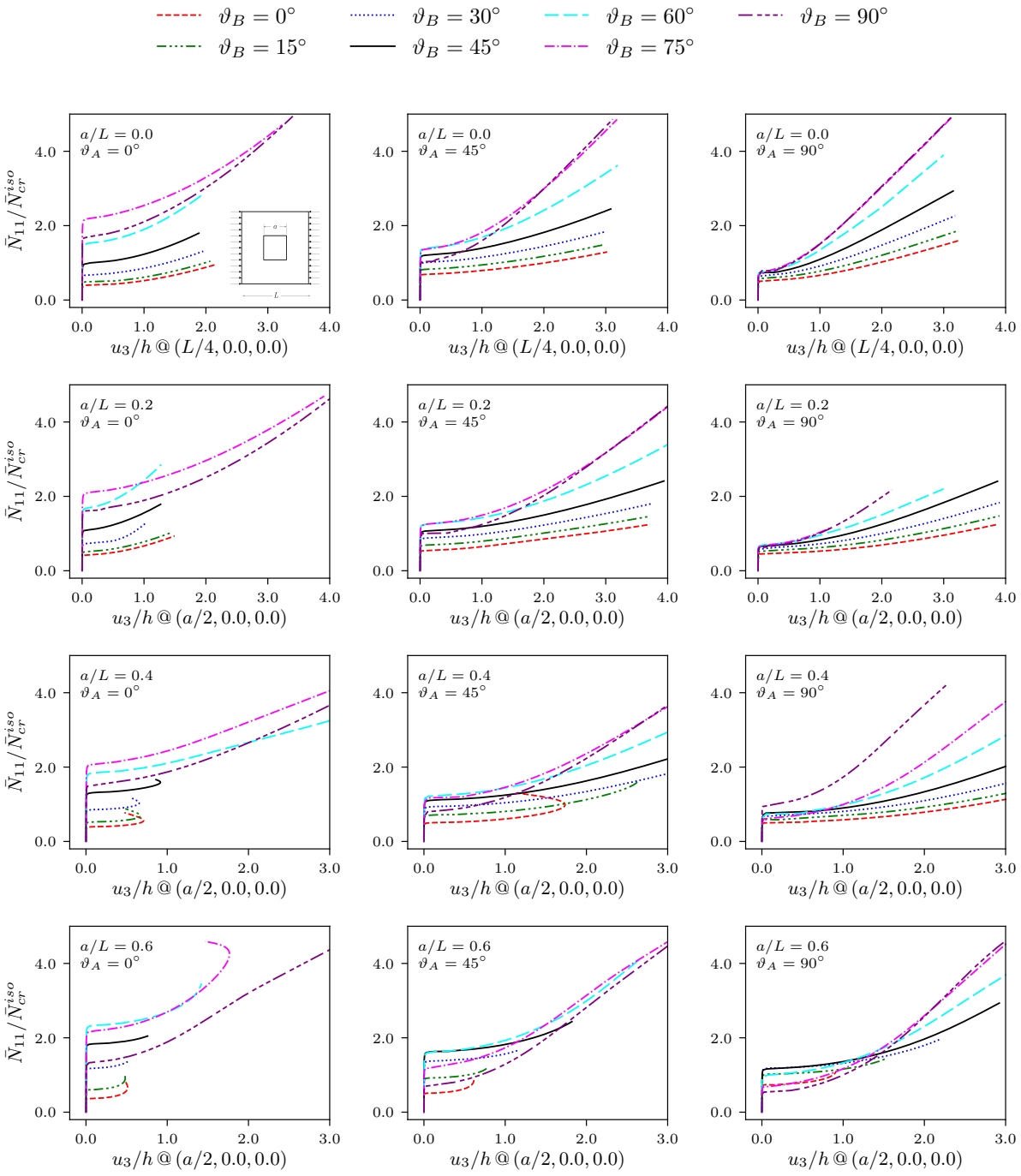

Figure 14: Load-displacement curves for VAT laminates with a central square cut-out having different dimension a/L.

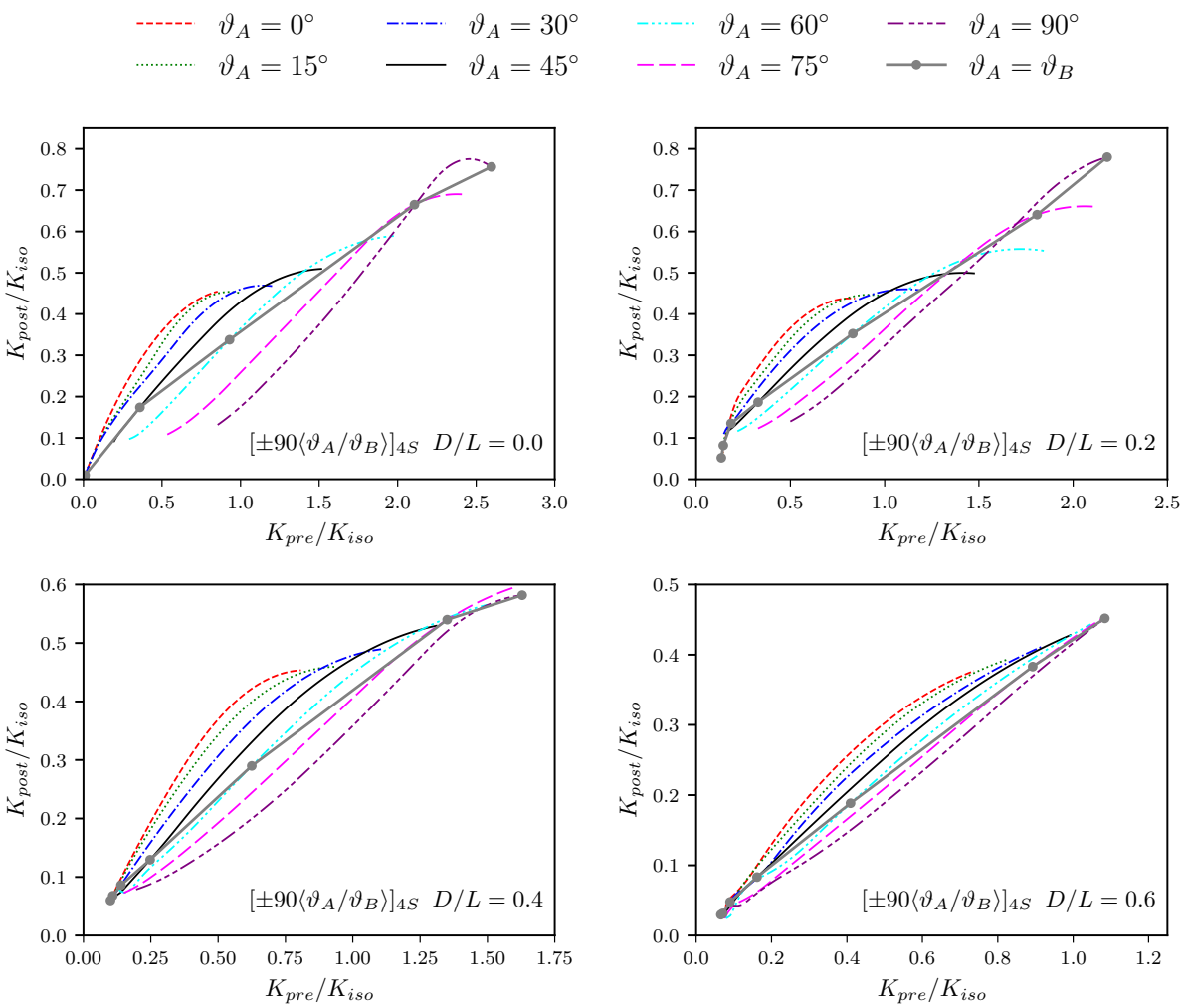

Figure 15: Variation of K_{pre} and K_{post} with respect to the ply fibre paths for the $[\pm(90\langle\theta_A/\theta_B\rangle)]_{4S}$ laminates.

theory in the framework of non-linear von Karman strains. The primary variables of the model, namely the plate mid-plane translations and transverse section rotations, are approximated by trial functions built as products of one-dimensional Legendre polynomials and the governing equations nonlinear system is inferred by the stationarity conditions of the plate energy functional. The cut-out geometry is implicitly defined via suitable level set functions, which enables the employment of an accurate special integration scheme for implicitly-defined domains. Numerical results are presented to validate the method for buckling and post-buckling analysis of variable stiffness plates with cut-outs, in particular they refer to the analysis of variable angle tow laminates. After validation, parametric investigations are proposed for buckling and post-buckling of variable angle tow laminates with cut-outs in order to show the capabilities of the proposed approach and establish some features of such structures. It is pointed out that the variable stiffness structural concept implemented via variable angle tow laminates allows to attain better buckling loads and post-buckling performances with respect to the straight fibres laminates. This circumstance widely reported in the literature for intact plates is here confirmed also for plates with cut-outs. In conclusion, it is affirmed that the developed method may provide a valuable tool for the analysis of variable stiffness laminated plates, whose design space is particularly wide and flexible allowing for improved structural performances.

6 Acknowledgements

The authors gratefully acknowledge the support of CINECA's staff for the use of CINECA's HPC facilities.

References

[1] J. Frketic, T. Dickens, S. Ramakrishnan, Automated manufacturing and processing of fiber-reinforced polymer (frp) composites: An additive review of contemporary and modern techniques for advanced materials manufacturing, Additive Manufacturing 14 (2017) 69–86.

[2] D. Punera, P. Mukherjee, Recent developments in manufacturing, mechanics, and design optimization of variable stiffness composites, Journal of Reinforced Plastics and Composites (2022).

[3] P. Ribeiro, H. Akhavan, A. Teter, J. Warmiński, A review on the mechanical behaviour of curvilinear fibre composite laminated panels, Journal of Composite Materials 48 (22) (2014) 2761–2777.

[4] Z. Xin, Y. Duan, W. Xu, T. Zhang, B. Wang, Review of the mechanical performance of variable stiffness design fiber-reinforced composites, Science and Engineering of Composite Materials 25 (3) (2018) 425–437.

[5] M. W. Hyer, R. F. Charette, Use of curvilinear fiber format in composite structure design, AIAA Journal 29 (6) (1991) 1011–1015.

[6] M. Hyer, H. Lee, The use of curvilinear fiber format to improve buckling resistance of composite plates with central circular holes, Composite Structures 18 (3) (1991) 239–261.

[7] D. Aditya Narayan, M. Ganapathi, B. Pradyumna, M. Haboussi, Investigation of thermo-elastic buckling of variable stiffness laminated composite shells using finite element approach based on higher-order theory, Composite Structures 211 (2019) 24–40.

[8] A. Viglietti, E. Zappino, E. Carrera, Analysis of variable angle tow composites structures using variable kinematic models, Composites Part B: Engineering 171 (2019) 272–283.

[9] Y. Yan, B. Liu, Y. Xing, E. Carrera, A. Pagani, Free vibration analysis of variable stiffness composite laminated beams and plates by novel hierarchical differential quadrature finite elements, Composite Structures 274, cited By 1 (2021).

[10] A. R. Sánchez-Majano, R. Azzara, A. Pagani, E. Carrera, Accurate stress analysis of variable angle tow shells by high-order equivalent-single-layer and layer-wise finite element models, Materials 14 (21) (2021) 6486. doi:10.3390/ma14216486.

[11] A. Sanchez-Majano, A. Pagani, M. Petrolo, C. Zhang, Buckling sensitivity of tow-steered plates subjected to multiscale defects by high-order finite elements and polynomial chaos expansion, Materials 14 (11) (2021).

[12] A. Pagani, A. Sanchez-Majano, Stochastic stress analysis and failure onset of variable angle tow laminates affected by spatial fibre variations, Composites Part C: Open Access 4 (2021).

[13] A. Pagani, R. Azzara, E. Carrera, Geometrically nonlinear analysis and vibration of in-plane-loaded variable angle tow composite plates and shells, Acta Mechanica (2022). doi:10.1007/s00707-022-03226-2.

[14] P. Hao, X. Yuan, C. Liu, B. Wang, H. Liu, G. Li, F. Niu, An integrated framework of exact modeling, isogeometric analysis and optimization for variable-stiffness composite panels, Computer Methods in Applied Mechanics and Engineering 339 (2018) 205–238.

[15] K. Liew, X. Zhao, A. J. Ferreira, A review of meshless methods for laminated and functionally graded plates and shells, Composite Structures 93 (8) (2011) 2031–2041.

[16] S. Castro, M. Donadon, T. Guimarães, Es-pim applied to buckling of variable angle tow laminates, Composite Structures 209 (2019) 67–78.

[17] D. Li, C. Featherston, Z. Wu, An element-free study of variable stiffness composite plates with cutouts for enhanced buckling and post-buckling performance, Computer Methods in Applied Mechanics and Engineering 371 (2020).

[18] G. Raju, Z. Wu, B. Kim, P. Weaver, Prebuckling and buckling analysis of variable angle tow plates with general boundary conditions, Composite Structures 94 (9) (2012) 2961–2970.

[19] G. Raju, Z. Wu, P. Weaver, Buckling analysis of variable angle tow composite plates using differential quadrature method, Journal of the Indian Institute of Science 93 (4) (2013) 689–698.

[20] R. Groh, P. Weaver, Buckling analysis of variable angle tow, variable thickness panels with transverse shear effects, Composite Structures 107 (2014) 482–493.

[21] F. Tornabene, N. Fantuzzi, M. Bacciocchi, Higher-order structural theories for the static analysis of doubly-curved laminated composite panels reinforced by curvilinear fibers, Thin-Walled Structures 102 (2016) 222–245.

[22] M. Rahmanian, T. Farsadi, H. Kurtaran, Nonlinear flutter of tapered and skewed cantilevered plates with curvilinear fiber paths, Journal of Sound and Vibration 500 (2021) 116021.

[23] A. F. Martin, A. W. Leissa, Application of the ritz method to plane elasticity problems for composite sheets with variable fibre spacing, International Journal for Numerical Methods in Engineering 28 (8) (1989) 1813–1825.

[24] Z. Wu, P. M. Weaver, G. Raju, B. Chul Kim, Buckling analysis and optimisation of variable angle tow composite plates, Thin-Walled Structures 60 (2012) 163–172.

[25] Z. Wu, G. Raju, P. M. Weaver, Postbuckling analysis of variable angle tow composite plates, International Journal of Solids and Structures 50 (10) (2013) 1770–1780.

[26] B. H. Coburn, Z. Wu, P. M. Weaver, Buckling analysis of stiffened variable angle tow panels, Composite Structures 111 (2014) 259–270.

[27] Z. Wu, G. Raju, P. M. Weaver, Optimization of postbuckling behaviour of variable thickness composite panels with variable angle tows: Towards "buckle-free" design concept, International Journal of Solids and Structures 132-133 (2018) 66–79.

[28] T. A. M. Guimaraes, S. G. P. Castro, C. E. S. Cesnik, D. A. Rade, Supersonic flutter and buckling optimization of tow-steered composite plates, AIAA Journal 57 (1) (2019) 397–407.

[29] R. Vescovini, L. Dozio, A variable-kinematic model for variable stiffness plates: Vibration and buckling analysis, Composite Structures 142 (2016) 15–26.

[30] V. Oliveri, A. Milazzo, A Rayleigh-Ritz approach for postbuckling analysis of variable angle tow composite stiffened panels, Computers and Structures 196 (2018) 263–276.

[31] V. Oliveri, A. Milazzo, P. Weaver, Thermo-mechanical post-buckling analysis of variable angle tow composite plate assemblies, Composite Structures 183 (1) (2018) 620–635.

[32] G. Sciascia, V. Oliveri, A. Milazzo, P. Weaver, Ritz solution for transient analysis of variable-stiffness shell structures, AIAA Journal 58 (4) (2020) 1796–1810.

[33] A. Milazzo, I. Benedetti, A non-linear Ritz method for the analysis of low velocity impact induced dynamics in variable angle tow composite laminates, Composite Structures 276 (2021).

[34] A. Milazzo, V. Oliveri, Investigation of buckling characteristics of cracked variable stiffness composite plates by an eXtended Ritz approach, Thin-Walled Structures 163 (2021).

[35] A. Milazzo, Free vibrations analysis of cracked variable stiffness composite plates by the extended ritz method, Mechanics of Advanced Materials and Structures (2022).

[36] C. Lopes, Z. Gürdal, P. Camanho, Tailoring for strength of composite steered-fibre panels with cutouts, Composites Part A: Applied Science and Manufacturing 41 (12) (2010) 1760–1767.

[37] V. S. Gomes, C. S. Lopes, F. F. A. Pires, Z. Gürdal, P. P. Camanho, Fibre steering for shear-loaded composite panels with cutouts, Journal of Composite Materials 48 (16) (2014) 1917–1926.

[38] A. Alhajahmad, C. Mittelstedt, Buckling and postbuckling performance of composite fuselage panels with cutouts using continuous streamline fibres, International Journal of Mechanical Sciences 212 (2021).

[39] M. Hachemi, S. Hamza-Cherif, A. Houmat, Free vibration analysis of variable stiffness composite laminate plate with circular cutout, Australian Journal of Mechanical Engineering 18 (1) (2020) 63–79.

[40] T. Shafighfard, E. Demir, M. Yildiz, Design of fiber-reinforced variable-stiffness composites for different open-hole geometries with fiber continuity and curvature constraints, Composite Structures 226 (2019) 111280.

[41] J. Fazilati, V. Khalafi, Effects of embedded perforation geometry on the free vibration of tow-steered variable stiffness composite laminated panels, Thin-Walled Structures 144 (2019).

[42] S. Ghannadpour, M. Mehrparvar, Energy effect removal technique to model circular/elliptical holes in relatively thick composite plates under in-plane compressive load, Composite Structures 202 (2018) 1032–1041.

[43] S. Ghannadpour, F. Rashidi, Efficient and accurate semi-analytical simulation of nonlinear behavior of imperfect variable stiffness plates containing rectangular holes, Thin-Walled Structures 171 (2022).

[44] V. Gulizzi, I. Benedetti, A. Milazzo, An implicit mesh discontinuous galerkin formulation for higher-order plate theories, Mechanics of Advanced Materials and Structures 27 (17) (2020) 1494–1508.

[45] V. Gulizzi, I. Benedetti, A. Milazzo, A high-resolution layer-wise discontinuous galerkin formulation for multilayered composite plates, Composite Structures 242 (2020) 112137.

[46] G. Guarino, V. Gulizzi, A. Milazzo, High-fidelity analysis of multilayered shells with cut-outs via the discontinuous galerkin method, Composite Structures 276 (2021) 114499.

[47] G. Guarino, A. Milazzo, V. Gulizzi, Buckling analysis of multilayered structures using high-order theories and the implicit-mesh discontinuous galerkin method, in: AIAA SCITECH 2022 Forum, 2022, p. 1490.

[48] J. Reddy, Mechanics of laminated composite plates and shells. Theory and analysis, CRC Press, 2004.

[49] A. Milazzo, V. Oliveri, Post-buckling analysis of cracked multilayered composite plates by pb-2 Rayleigh-Ritz method, Composite Structures 132 (2015) 75–86.

[50] A. Milazzo, V. Oliveri, Buckling and postbuckling of stiffened composite panels with cracks and delaminations by Ritz approach, AIAA Journal 55 (3) (2017) 965–980.

[51] S. N. Chatterjee, S. V. Kulkarni, Shear correction factors for laminated plates, AIAA Journal 17 (5) (1979) 498–499.

[52] Z. Gürdal, B. Tatting, C. Wu, Variable stiffness composite panels: Effects of stiffness variation on the in-plane and buckling response, Composites Part A: Applied Science and Manufacturing 39 (5) (2008) 911–922.

[53] J. Reddy, Energy Principles and Variational Methods in Applied Mechanics, John Wiley & Sons, 2002.

[54] M. A. Crisfield, Non-Linear Finite Element Analysis of Solids and Structures, John Wiley & Sons, 1991.

[55] T. Yang, A. Qarariyah, H. Kang, J. Deng, Numerical integration over implicitly defined domains with topological guarantee, Communications in Mathematics and Statistics 7 (4) (2019) 459–474.

[56] R. I. Saye, High-order quadrature methods for implicitly defined surfaces and volumes in hyperrectangles, SIAM Journal on Scientific Computing 37 (2) (2015) A993–A1019.

[57] R. Saye, Implicit mesh discontinuous galerkin methods and interfacial gauge methods for high-order accurate interface dynamics, with applications to surface tension dynamics, rigid body fluid–structure interaction, and free surface flow: Part i, Journal of Computational Physics 344 (2017) 647–682.

[58] R. Saye, Implicit mesh discontinuous galerkin methods and interfacial gauge methods for high-order accurate interface dynamics, with applications to surface tension dynamics, rigid body fluid–structure interaction, and free surface flow: Part ii, Journal of Computational Physics 344 (2017) 683–723.

[59] R. Saye, Fast multigrid solution of high-order accurate multiphase stokes problems, Communications in Applied Mathematics and Computational Science 15 (2) (2020) 147–196.

[60] V. Gulizzi, A. S. Almgren, J. B. Bell, A coupled discontinuous galerkin-finite volume framework for solving gas dynamics over embedded geometries, Journal of Computational Physics 450 (2022) 110861.

[61] V. Gulizzi, R. Saye, Modeling wave propagation in elastic solids via high-order accurate implicit-mesh discontinuous galerkin methods, Computer Methods in Applied Mechanics and Engineering 395 (2022) 114971.

[62] A. Milazzo, I. Benedetti, A non-linear ritz method for the analysis of low velocity impact induced dynamics in variable angle tow composite laminates, Composite Structures 276 (2021).

[63] M. D. Pandey, A. N. Sherbourne, Postbuckling behaviour of optimized rectangular composite laminates, Composite Structures 23 (1993) 27–38.

A Appendix

The expressions of the implicit level set functions employed for basic cutouts are provided in this appendix. They are expressed in the plate domain coordinates x_1 and x_2

A.1 Circular cutout

Considering a circular cutout, the level set function is expressed as

$$\phi = R^2 - (x_1 - \bar{x}_1)^2 - (x_2 - \bar{x}_2)^2 \tag{25}$$

where R is the radius and $\bar{x}_1$ and $\bar{x}_2$ are the centre coordinates.

A.2 Elliptical cutout

Let us consider an elliptical cutout. With reference to the geometrical quantities defined in Fig. 16a, the employed level set function is given by

$$\phi = 1 - \frac{\left[(x_1 - \bar{x}_1)\cos\beta + (x_2 - \bar{x}_2)\sin\beta\right]^2}{a^2} - \frac{\left[(x_2 - \bar{x}_2)\cos\beta - (x_1 - \bar{x}_1)\sin\beta\right]^2}{b^2} \tag{26}$$

A.3 Rectangular cutout

The level set function for a rectangular cutout with rounded corners is given by

$$\phi = \left(\frac{a}{2}\right)^d - \left[-\frac{(x_2 - \bar{x}_2)\cos\beta - (x_1 - \bar{x}_1)\sin\beta}{r}\right]^d - \left[(x_1 - \bar{x}_1)\cos\beta + (x_2 - \bar{x}_2)\sin\beta\right]^d \tag{27}$$

where the involved quantities are defined in Fig. 16b, $r = b/a$ and the exponent d determines the corner fillet radius. It is worth noting that high values of d provide low corner fillet radius; in the examples proposed in the present paper it was set $d = 100$ which actually simulate sharp corners.

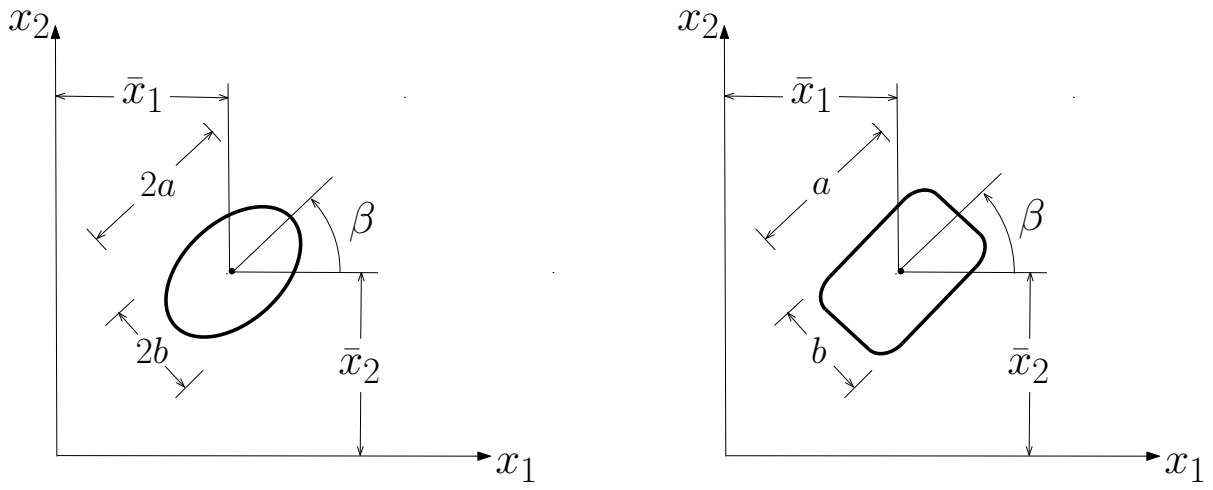

(a) Elliptical.

(b) Rectangular

Figure 16: Cut-out geometry.